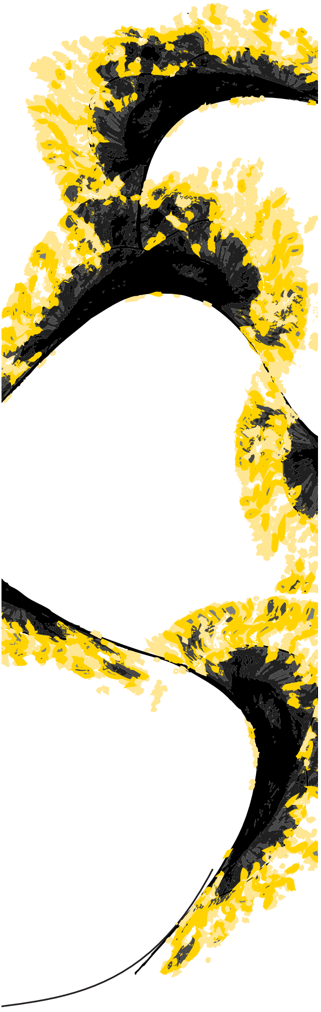

RAM. ROBOTICS AND MECHATRONICS

DESIGN, FABRICATION AND EVALUATION OF A 3D PRINTED SOFT ROBOTIC ACTUATOR WITH EMBEDDED SENSING

S.Y. (Stijn) Kolkman

BSC ASSIGNMENT

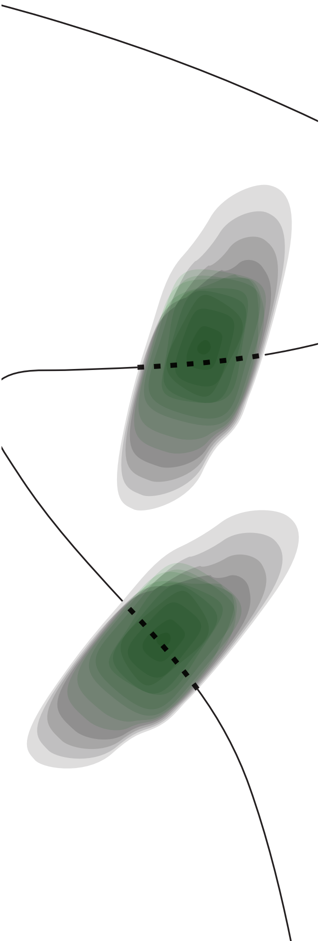

Committee:
prof. dr. ir. G.J.M. Krijnen
dr. ir. G.J.W. Wolterink
dr. A. Sadeghi

July, 2022

022RaM2022
Robotics and Mechatronics
EEMCS
University of Twente
P.O. Box 217
7500 AE Enschede
The Netherlands

UNIVERSITY OF TWENTE. | TECHMED CENTRE
UNIVERSITY OF TWENTE. | DIGITAL SOCIETY INSTITUTE

Abstract

In the field of soft robotics, researchers want to mimic the movement of soft bodies found in nature. Soft robots have the unique advantage to be able to adapt to the shape of the object they are touching and are thus often safer while working in human environments. It is however still difficult to measure the position of such a soft body accurately using internal sensors. The significant development in 3D printing technology has made it possible to print soft robots with embedded sensors.

This work shows the design, fabrication and characterisation of a 3D printed pneumatic soft robotic actuator with embedded strain gauges to determine the bending angle of the actuator. The actuator and strain gauges have been printed in one go using a multi material FFF printer. The actuator contains two strain gauges such that a differential measurement can be performed.

The fabricated actuator is able to bend approximately 180° and can apply a force of around 3 N at 0.3 MPa pressure. The differential signal of the embedded strain sensors shows an reasonable linear relation to the bending angle, while the response of each individual sensor is non-linear due to the nature of the strain gauge material. The proposed model of the actuator is based on the Euler Bernoulli beam theory. The model is however limited in describing the large deflections of the actuator.

Based on this research a paper has been written for the IEEE SENSORS 2022 conference. This paper can be found in appendix A

Contents

1 Introduction

1.1 Problem Statement

Robots operate in pre-shaped environments, allowing them to work fast. However, conventional robots are only able to perform the specific task they are programmed for. An upcoming new field in robotics is soft robotics [1]. In the field of soft robotics, researchers want to mimic the movement of soft bodies found in nature, such as snakes or octopuses. Soft robots have the unique advantage to be able to adapt to the shape of the object they are touching. Because of this, soft robots are often safer while working in human environments, e.g. while working as service robot.

Over the last few years 3D printing technology has seen much development. The versatility and easy customisation of 3D printing enables it to compete with traditional manufacturing methods in certain situations, e.g. for rapid prototyping [2]. New 3D printing materials have been developed. Especially the development of soft and flexible materials with electrical conductivity can be useful for the production of soft robots. Using multi-material 3D printing, sensors and actuators can be embedded in soft robots in a single fabrication process.

One of the main problems with soft robotic actuators is measuring the position accurately using internal sensors, such that their position can be controlled using closed-loop control [3]. Embedding flexible sensors in these soft robotic actuators using multi-material 3D printing can help to solve this problem.

1.2 Related Work

In the Netherlands the Dutch Soft Robotics Consortium is a group of researchers who are researching various aspects of soft robotics. Four universities; TU Delft, Eindhoven University of Technology, University of Twente and Wageningen University & Research, work together and learn from solutions in nature to create soft robots with embedded sensors and actuators [1]. At the Robotics and Mechatronics (RAM) research group at the University of Twente multiple types of 3D printed sensors have already been made. Wolterink et al. [4] have for example made a 3D printed strain sensor to measure the normal and shear components of an interaction force on a finger. This sensor was flexible and easy to fabricate in one-go using a multi material FFF printer. However this 3D printed sensor showed a high level of drift and non-linearities. These non-linearities are often seen in 3D printed sensors and multiple methods have been used to limit this effect. Schouten et al. [5] used differential measurements to linearise the output of a 3D printed tactile sensor. But also regression and neural networks have been used to linearise these sensors [4, 6].

Different attempts have already been made in fabricating soft robotic actuators [7]. Franke et al. [8] e.g. have made a dielectric elastomer bending actuator. This actuator however has multiple fabrication steps and is not fully 3D printable. Elgeneidy et al. [6] have made a pneumatic fully 3D printable actuator with embedded strain gauge. Their design, however, needed an additional fabrication step to combine the actuator with the sensor and showed a high level of hysteresis due to the use of one strain sensor.

1.3 Scope of This Thesis

In order to control a soft robotic actuator, its position needs to be accurately determined. This can be done by placing a sensor on the outside of the actuator. Recent developments in 3D printing make it now possible to 3D print sensors and to embed them in the actuators. Therefore the goal of this research is to develop and characterise a soft robotic actuator with embedded sensing, that can determine the position of the actuator using its mechanical deformation. From this goal the following research question has arisen:

> *What is the best way to embed a 3D printed sensor in a soft robotic actuator to measure the deflection?*

1.4 Report Structure

This report is divided into seven chapters. In this first chapter a brief introduction is given and the goal and research question are presented. In chapter two the design of the actuator is discussed after which in chapter three the design of the sensor, which will be embedded into the actuator, will be discussed. The fourth chapter is about which methods are used to fabricate and characterise the actuator and sensor. A model for the actuator and sensor will also be discussed in this chapter. In chapter five the results of the characterisation are presented. These results will be discussed in chapter six. After which in the last chapter, chapter seven the conclusions from this research are drawn.

2 Actuator Design

2.1 Introduction

In this chapter, the steps that have been taken to design a soft robotic actuator are explained. First the actuator requirements will be stated, after which the different types of soft actuators are compared. Based on the stated requirements and the properties of these different types of soft actuators, one type will be chosen and further investigated. Lastly, the design of the actuator, based on introduced theory, will be presented and all the main features will be described.

2.2 Actuator Requirements

The actuator that will be designed must fulfil the requirements stated below to reach the goal: "To develop and characterise a soft robotic actuator with embedded sensing, that can determine the position of the actuator using its mechanical deformation" as stated in Chapter 1.

- The actuator should only bend in one direction, bending/expanding in other directions should be minimised.
- The bending angle of the actuator should be controllable by a single input parameter that is supplied to the actuator.
- The actuator should be fabricated using FFF 3D printing.

2.3 Types of Soft Robotic Actuators

Multiple principles can be used to make a bending actuator. These can be divided in 5 main classes based on their actuation type [7]:

- *Electrically actuated.* Using materials, such as piezoelectric materials, that can transform electrical energy into mechanical energy, soft actuators can be made which are very responsive [9]. However, most of these actuators require a high voltage to work correctly.
- *Magnetically actuated.* By applying an external magnetic field all kinds of magnetic mediums can be actuated. Needing an external magnetic field can both be an advantage and a disadvantage [10]. Having the magnetic field externally can save a lot of space while operating in enclosed areas.
- *Thermally actuated.* These type of actuators are made of materials which deform by applying a certain amount of thermal energy [11]. These actuators tend to react slowly and are not energy efficient.
- *Photo-responsive.* These actuators can convert the energy available in light to a mechanical deformation [12]. Generally, this type of actuator also reacts slowly and is not energy efficient.
- *Pressure driven.* Using a pressurised gas a deformation can be generated and by carefully designing, these deformations can be used to make an actuator which moves in the desired directions [13]. These actuators can produce high forces, are energy efficient and react fast.

2.3.1 Chosen Actuator Type

Since the actuator needs to be made from a material which can be 3D printed using an FFF 3D printer, photo-responsive and thermally stimulated actuators are not an option. Magnetically stimulated is also not desired since it requires an external magnetic field to work correctly.

Electrically stimulated and pressure driven actuators can both produce a high force and are very responsive [9, 13]. However, because of the required high voltage needed for electrically stimulated actuators, it has been decided to make a pressure driven actuator.

2.4 Pneu-net Actuators

One of the most researched types of pressure driven bending soft actuator, is the pneu-net actuator [14]. These pneu-nets are actuated by pressurising a pneumatic network of chambers made from an elastic material. pneu-nets have been developed by the Whiteside Research Group at Harvard [15]. They have developed two types of pneu-nets of which the designs can be seen in Figure 2.1.

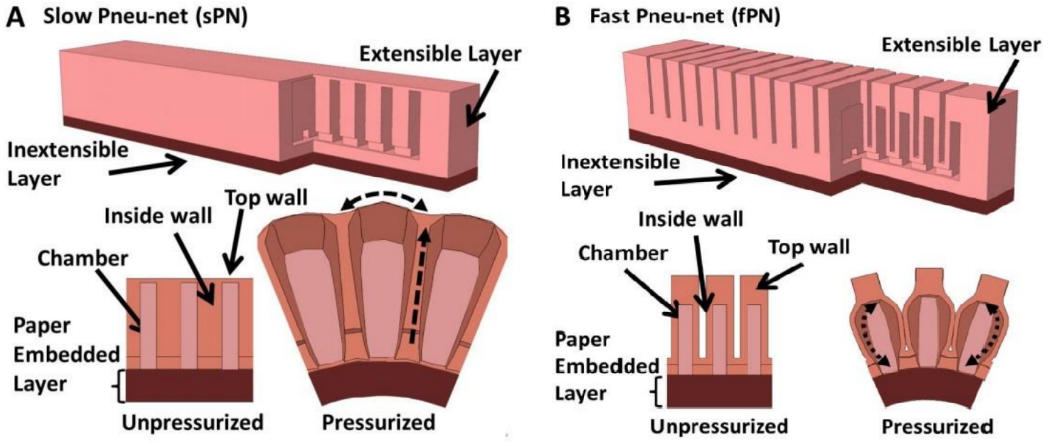

Figure 2.1: Design overview of the 2 most seen pneu-net actuators: A. Slow pneu-net (sPN). B. Fast pneu-net (fPN) [14].

The first pneu-net type they developed is called the slow pneu-net (sPN). This type of pneu-net exists of a thin layer of inextensible but flexible material on which a thicker layer of extensible material is placed. In this layer, multiple chambers are present in the length direction. When pressurised, these chambers expand and cause the actuator to bend. These slow pneu-nets usually require a change in volume of twenty times their initial volume to achieve their full range of bending. That is why a new type of pneu-net has been developed, the fast pneu-nets (fPN). These pneu-nets are based on the design of slow pneu-nets, but have a thicker top wall and have a gap in between the chambers. This results in the inside walls of the chambers to expand when pressurised and to push against each other. This produces a force which bends the actuator. Fast pneu-nets are faster, can exert more force and need less compressed air to operate with respect to slow pneu-nets, which means a smaller compressor can be used. For this research, the design of a fast pneu-net is used because of the previous explained advantages.

2.5 Actuator Design

When designing a pneu-net actuator, there are many dimensions that can be optimised to ensure the largest bending for a certain pressure, e.g. the height of the chambers. To calculate the optimal dimensions, analytical models could be useful. However, it is difficult to analytically model the behaviour of these actuators since these actuators have complex (deformation) shapes. Often these actuators are also made of hyperelastic materials which have a non-linear stress strain relationship, which is difficult to model analytically [16]. Usually experiments or finite element models are used to find the optimal shape [17]. This is however out of scope of this research, since more focus is put on embedding a sensor in the actuator. The dimensions of this design are based on the design made by Mosadegh et al. [14, 15] and are optimised such that the actuator could be manufactured using an FFF 3D printer.

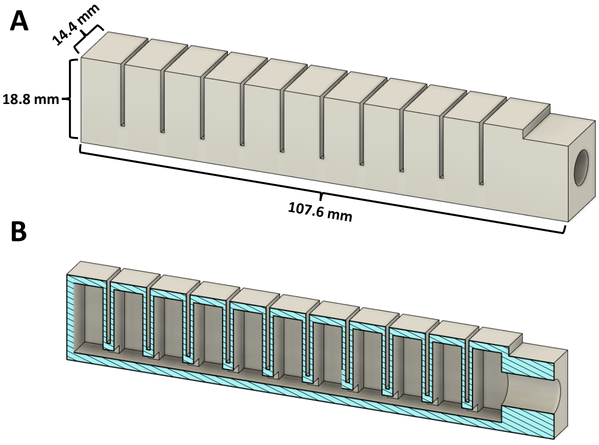

Figure 2.2: A. An overview of the designed actuator (based on the fast pneu-net (fPN) actuator). B. Section view of the actuator.

A render of the designed actuator is shown in Figure 2.2. The design is based on a fast pneu-net. The dimensions of the total actuator are 107.6 mm by 14.4 mm by 18.8 mm (length x width x height). The pneu-net has 11 chambers which have an inner dimension of 6.4 mm by 11.2 mm by 15.4 mm (length x width x height). The gap between the chambers is made as small as possible, such that it can still be manufactured. This will ensure the largest bending. The walls between the chambers are 0.8 mm thick and all the other walls of the chambers are 1.6 mm thick. Because the walls between the chambers are thinner, these will expand more than the other walls, which will again help the actuator to bend even more efficient since less energy will be lost in the expanding of the other walls. The floor of the actuator is 1.8 mm thick. In this floor a sensing structure will be embedded.

In the base of the actuator there is a hole with a radius of 3.75 mm. In this hole a pneumatic fitting can be pressed such that a tube can be connected to the actuator. Through this tube the compressed air will be supplied. The air can freely move between the chambers because of the small hole between the chambers above the bottom wall. This hole has a rectangular shape since Wang et al. [18], using finite element models and experiments, discovered that either a rectangular or semicircle shape would ensure the largest bending. A rectangular shape is chosen since this is easier to fabricate using an FFF 3D printer.

2.6 Conclusion

First the requirements for the soft actuator have been formulated in this chapter. Then by comparing the different actuation principles it was decided to make a pressure driven actuator, since this type of actuator can operate fast, produces high forces and is energy efficient. The specific pressure driven actuator that has been designed is a pneu-net actuator. The design of this the actuator can be seen in Figure 2.2.

3 Sensing Structure Design

3.1 Introduction

In the previous chapter the design of the actuator was introduced. This chapter will focus on the development of the sensing structure. After the requirements for the sensing structure have been stated, the different types of 3D printable sensors will be compared and one of these types will be chosen based on the requirements of the sensing structure. In the end, the design of the sensing structure will be presented and discussed.

3.2 Sensing Structure Requirements

Before designing the sensing structure, the requirements for the sensing structure need to be determined. The requirements stated below must be met in order to reach the goal: "To develop and characterise a soft robotic actuator with embedded sensing, that can determine the position of the actuator using its mechanical deformation" as stated in section Chapter 1.

- The sensing structure should be able to measure the bending angle of the actuator.
- The sensing structure should only be sensitive to a change in the bending angle.
- The sensing structure should have a negligible influence on the bending performance of the actuator.
- The sensing structure and pneu-net should be fully 3D printable in one go using a multi-material FFF printer.

3.3 Sensing Structure Type

3.3.1 3D Printed Sensor Types

Three types of 3D printed sensors are often used, piezoresistive, capacitive and inductive sensors [2].

- *Piezoresistive sensors.* One of the most used methods to measure forces and deflections is by making use of the piezoresistive effect of conductive 3D printable materials. Wolterink et al. [19] demonstrated the use of a 3D printed strain sensor to measure the normal and shear components of an interaction force on a finger. 3D printed strain sensors have the advantage that they are flexible, easy to fabricate and easy to readout. However, this comes at a cost: strain sensors show a high level of drift and non-linearities [2]. There are methods to reduces this effect e.g. Schouten et al. [5] showed the effect of differential strain measurement in 3D printed sensors. Due to this differential measurement the linearity of the response function was highly improved. Compensation models can also be used to overcome these non-linearities. Elgeneidy et al. [6] for example used regression, Wolterink et al. [20] used an neural network and Kosmas et al. [21] used a modified Power Law Model (mPLW).
- *Capacitive sensors.* Another type of sensor that can be 3D printed is a capacitive sensor. These sensors consist of a parallel plate capacitor made of a conducting material with a dielectric in between [2]. This sensor type has the advantage that it shows a low level of drift and non-linearities. However, to work correctly these sensors need to be shielded to reduce the effect of parasitic capacitances. These sensors are mostly used for measuring normal forces [22], but can also be used to measure deflections [23].
- *Inductive sensors.* Lastly, inductive sensors can be used in 3D printed structures. However, this type of sensor is not used that often since most conductive filaments which are

on the market are not conductive enough to serve as an inductor (resistivity of several Ωcm [24]). Some attempts have been done to make inductors using conductive filaments [25], which resulted in inductors with an inductance of several microhenry (µH). Another option would be to embed copper or nickel wires into the 3D printed structure [26] or by using silver paste [27] or liquid metal.

3.3.2 Selection of Sensor Principle

To measure the deflection angle of the actuator, a piezoresistive sensor was chosen, since this type of sensor is the easiest to implement and has proven to be able to measure forces and angles [5,6,19]. A capacitive sensor would also be an option, especially since this type of sensor has a low level of drift and non-linearities, however, this type of sensor would need shielding in order to work correctly and would require more complex readout hardware. An inductive sensor is out of scope, since there are no 3D printable materials which are conductive enough and can be printed using an FFF printer (only carbon infused polymers are available, but these have a resistivity of several Ωcm [24]).

3.3.3 Strain Gauges

Strain gauges are sensors which (among other things) make use of the piezoresistive effect. Strain gauges can measure the resistance change that is caused by a deformation of the material [28]. When a strain gauge is elongated both the piezoresistive effect and the shrinkage of the cross-section, normally cause the resistance of the gauge to go up. The opposite happens when the strain gauge is compressed. An import factor for the performance of a strain gauge is the gauge factor (GF) [4]. The gauge factor is the ratio of relative change in electrical resistance ($\frac{\Delta R}{R_0}$) to the mechanical strain (ϵ):

$$GF = \frac{\frac{\Delta R}{R_0}}{\frac{\Delta L}{L_0}} = \frac{\frac{\Delta R}{R_0}}{\epsilon} \tag{3.1}$$

In Figure 3.1 a simple design of a strain gauge is shown. A strain gauge exists of two connection pads and a sensitive region. Due to the design of this strain gauge, the strain gauge is the most sensitive to deformations in the horizontal direction.

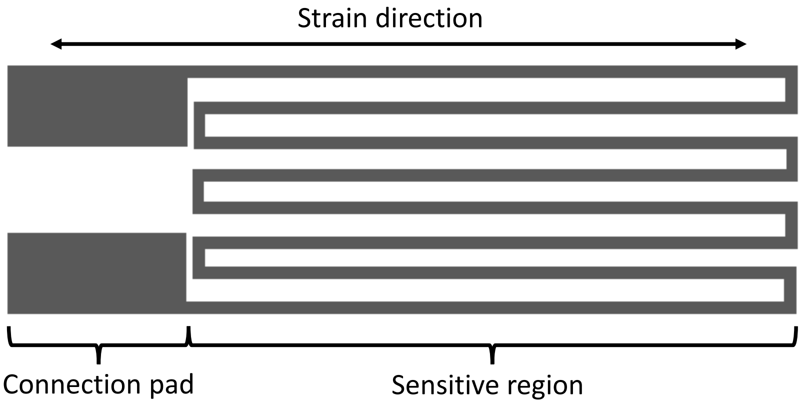

Figure 3.1: Simple strain gauge design seen from the top.

3.4 Compensating for Non-linearities

As earlier stated in section 3.3.1, 3D printed strain sensors show a high level of drift and non-linearities [2]. In Figure 3.2 the relative resistance change ($\frac{\Delta R}{R_0}$) of a conductive 3D printable material (conductive TPU) at various strain rates can be seen. It can clearly be seen that the relation between the relative change in resistance and the strain is non-linear. For a strain between 0-0.1 the gauge factor is roughly -15 (the blue dotted line in Figure 3.2). For higher levels of strain the gauge factor is approximately zero. Wolterink et al. [4] noted that the initial drop in resistance at low strain values is probably related to the alignment of conductive carbon black particles in the TPU material and that higher strains can cause these networks to break down which results in an increase in resistance.

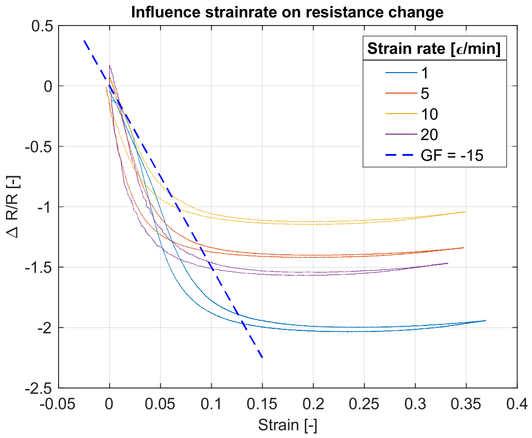

Figure 3.2: Relative resistance change ($\frac{\Delta R}{R_0}$) of a conductive 3D printable material (conductive TPU) at various strain rates. Adapted from [4].

To overcome these non-linear effects compensation models could be used such as already given in section 3.3.1. However, these algorithms can be very complex, a more straightforward approach that can help make the output more linear is by using a differential measurement [29]. Schouten et al. [5] used this to linearise the output of a 3D printed flexible, piezoresistive, tactile sensor.

Differential measurements can be done when using two sensors which measure the same parameter but with opposite sign. Schouten et al. [5] showed that the response of these two sensors (y_1 and y_2) can be written as :

$$y_1 = f(x) \tag{3.2}$$

$$y_2 = f(-x) \tag{3.3}$$

Where x is the input of the sensor, y_1 and y_2 are the outputs and f is the function which relates the output of the sensor to the input parameter of the sensor. This can be approximated by a power series:

$$y_1(x) = \sum_{\mathrm{n}=0}^{\infty} a_{\mathrm{n}} x^n \tag{3.4}$$

$$y_2(x) = \sum_{\mathrm{n}=0}^{\infty} a_{\mathrm{n}} (-x)^n \tag{3.5}$$

Then the differential measurement of these two sensors with opposite signs will give:

$$z = y_1(x) - y_2(x) \tag{3.6}$$

$$z = \sum_{\mathrm{n}=0}^{\infty} a_{\mathrm{n}} x^n - \sum_{\mathrm{n}=0}^{\infty} a_{\mathrm{n}} (-x)^n \tag{3.7}$$

$$z = \sum_{\mathrm{n}=0}^{\infty} 2 a_{\mathrm{n}} x^{2\mathrm{n}+1} \tag{3.8}$$

For all even powers, the signals of the two sensors have the same coefficients. When subtracting these signals from each other, these even powers are removed. By removing these higher-order terms, the linearity of the sensor is increased. Using a differential measurements also any drift that both sensors experience can be removed. Drift in strain sensors is caused by e.g. a temperature or humidity change. Here it is assumed that both sensors are the same and have the same response function f. This is however in reality often not the case, which can result in the drift and non-linearities to only partially be removed. Therefore, care must be taken that both sensor will have the same properties.

3.5 Sensing Structure Design

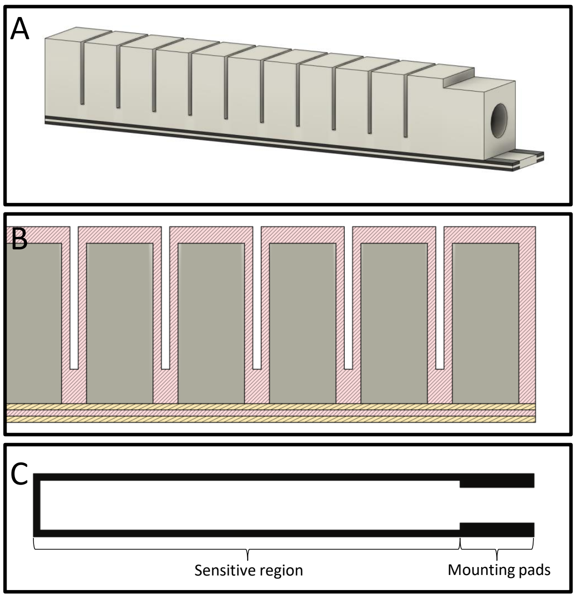

Figure 3.3: A. Actuator one (white) including the sensing structure (black). B. Section view of the actuator including sensing structure. The two yellow parts in the bottom layer are the sensing structure. C. Shape of 1 sensor (topview).

Using the previously explained theory, the sensing structure has been designed. The design can be seen in Figure 3.3. It consists of two strain gauges in the bottom layer of the actuator such that a differential measurement can be done. It is expected that the neutral axis will be in the middle of the bottom layer of the actuator. To ensure that both strain gauges give the same response but with opposite signs, they are placed the same distance above and below the neutral axis. To test the hypothesis that the neutral axis is in the middle of the bottom layers, also one actuator has been designed which has the top strain gauge higher above the expected neutral axis than the bottom sensor below the neutral axis. If the distance to the top sensor is larger, this sensor will also experience a higher strain and thus have a larger amplitude (the relation between the strain and the distance above the neutral axis will be derived in Section 4.3).

The actuator with the sensors at an equal distance to the expected neutral axis will be called "actuator one" and the other "actuator two" in the remaining chapters.

The design is optimised to measure the bending of the actuator. When bent, the largest strain will be in the length direction of the actuator, so the sensitive part of the gauge will also be placed in this direction. For connecting the sensors to the measurement setup, each sensor has two mounting pads. The mounting pads have a larger cross-section such that they have a low resistance and thus have a small influence on the total resistance of the strain gauge. This larger cross-section also has the advantage that wires can more easily be attached to the sensing structure later.

As will be explained in Section 4.2, the layer height with which the sensing structure will be printed is 0.15 mm and the extrusion width is 0.4 mm. The dimensions of the sensor have been optimised for these printer settings, by making the dimension of the sensing structure a multiply of these printing parameters. This way the printed lines and layers will neatly align. Each strain gauge is 0.6 mm thick (4 layers) and the active region of the strain gauge has a width of 1.6 mm (4 traxels). By making the strain gauge 4 traxels width and thick, possible defects in a traxel can be (partly) compensated for by the surrounding traxels. The length of the sensing structure is limited by the length of the actuator. The sensing structure is placed over the whole length to make sure that any bending at any point on the actuator can be measured.

As shown in Figure 3.3.A, the strain gauge is placed as close to the outside wall as possible. This has been done since it was found in an earlier design that the bottom layer of the actuator bulges when the actuator is pressurised. This bulging puts an additional strain on the sensors. Both sensors will experience this strain and because of the differential measurement, this strain probably will not influence the differential sensor output that much. However, it was still chosen to place the sensing structure as close to the outside wall as possible, where the strain due to bulging will be the lowest, and thus the influence of this bulging on the sensor output will be minimal.

3.6 Conclusion

After formulating the requirements of the sensing structure (with the main requirement that the sensing structure should be able to measure the bending angle of the actuator), different types of 3D printable sensing structures were compared (piezoresistive, capacitive and inductive). It was decided to design a piezoresistive sensing structure. The designed sensing structure can be seen in Figure 3.3. The design consists of two strain gauges such that differential measurements can be done.

4 Method

4.1 Introduction

This chapter explains the used fabrication and characterisation methods. First, the steps taken to print and post process the actuator with sensors will be explained. Hereafter, the analytical model of the actuator and sensor will be derived. Lastly, the actuator and sensor characterisation methods will be explained.

4.2 Fabrication

4.2.1 Actuator and Sensor Materials

The actuator needs to be made from a flexible material such that the chambers can expand and the actuator can bend. The most used type of flexible material that can be 3D printed is thermoplastic polyurethane (TPU). For this actuator, NinjaFlex (NinjaTek, Manheim, PA, USA) is used. NinjaFlex is and flexible and durable TPU [30].

The sensing structure must be made from a conducting material. The material must also be flexible since it will need to bend in the same shape as the actuator. The chosen material that has these properties is PI-eTPU 85-700+ (Palmiga Innovation, Sweden) [31].

4.2.2 FFF 3D Printer

For 3D printing the actuator and sensor in one go, a 3D printer is needed that can print both flexible and conducting materials, since the actuator will be made from a material which is flexible and the sensor from a material which is both flexible and conducting. The used printer that is able to do this, is the Diabase H-Series (Diabase Engineering, Longmont, CO, USA) multi-material FFF 3D printer.

This printer has a rotary toolhead with 5 Bondtech extruders (Bondtech LGX, Bondtech AB, Sweden), such that 5 different materials can be printed per print job. These extruders are able to print all kind of materials, including flexible and conductive materials. The printer and a detailed view of the rotary toolhead can be seen in Figure 4.1.

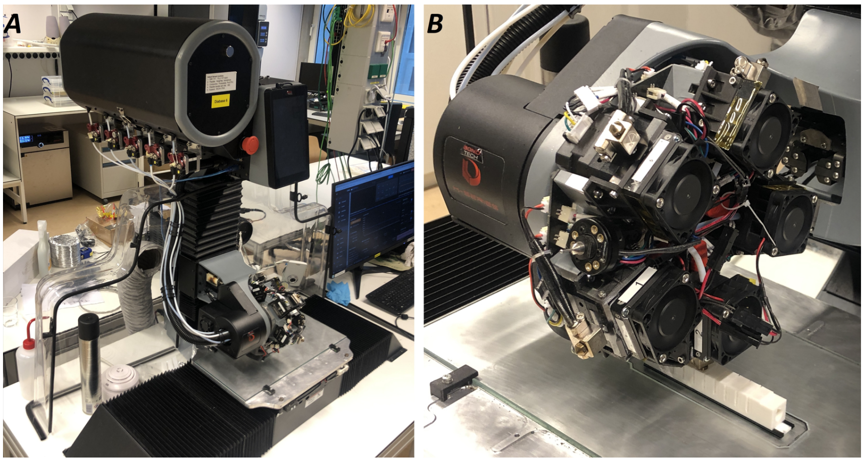

Figure 4.1: A. Diabase H-Series multi-material FFF 3D printer. B. Detailed view of the rotary toolhead.

Table 4.1: Slicer settings

Parameter	**TPU**	**ETPU**
Extrusion multiplier	1.30	1.00
Nozzle diameter	0.4 mm	0.4 mm
Layer height	0.15 mm	0.15 mm
Infill	100 %	100 %
Infill pattern	Rectilinear	Rectilinear
Temperature	225°	215°
Printing speed	2000 mm/min	2000 mm/min
Outline/perimeter shells	3	3

4.2.3 Designing and Slicing

The model is designed in Fusion 360 (Autodesk, San Francisco, CA, USA) [32]. In Fusion 360 a separate component is made for the sensor and for the actuator. These components are then exported to the slicer software. For slicing Simplify3D (Simplify3D, Cincinnati, OH, USA) has been used. The used slicer settings are shown in Table 4.1

Most of the settings are the recommended settings for the corresponding material [30,31]. The layer height was set to 0.15 mm. 0.15 mm was found to be a high enough resolution while also keeping the printing time reasonable. For the TPU an extrusion multiplier of 1.30 is used. This over-extruding makes the actuator more airtight. The number of outline/perimeter shells was set to 3. This is the number of walls that will be printed before the infill pattern is started. Setting this value to 3 will make sure that the walls of the chambers consist of aligned traxels, which is again found to be beneficial for airtightness.

Lastly, a prime pillar and skirt are enabled. These will ensure that the nozzles are primed before they start depositing a new layer on the model such that there is a smooth transition between the TPU and conductive TPU. A finished print with these printer settings can be seen in Figure 4.2.

Figure 4.2: The actuator on the heated bed directly after printing. On the left the prime pillar can be seen. Also a skirt can be seen around the actuator.

4.2.4 Post Processing

After printing several strings were present between the chambers as seen in Figure 4.3.A. These strings form during the printing process when the printer head moves between the chambers and still some filament is coming out of the nozzle. These strings are not beneficial for the bending behaviour of the actuator, so these strings are removed using a knife. Furthermore, the actuator is annealed for 15 hours at 80 °C. This annealing will make the sensors behaviour more stable and also lowers the resistance of the sensors [4]. A connector (FESTO Cartridge QSPK10-4) is pressed in the 7.5 mm hole, to which later a 4 mm tube can be attached, through which the compressed air will be transported. Lastly, two wires are connected to each sensor by melting the ends of the wires into the mounting pads using a soldering iron, this is shown in Figure 4.3.B. The other ends of the wires are soldered to a connector such that the sensor can be connected to the measurement setup. A finished actuator is shown in Figure 4.3.C.

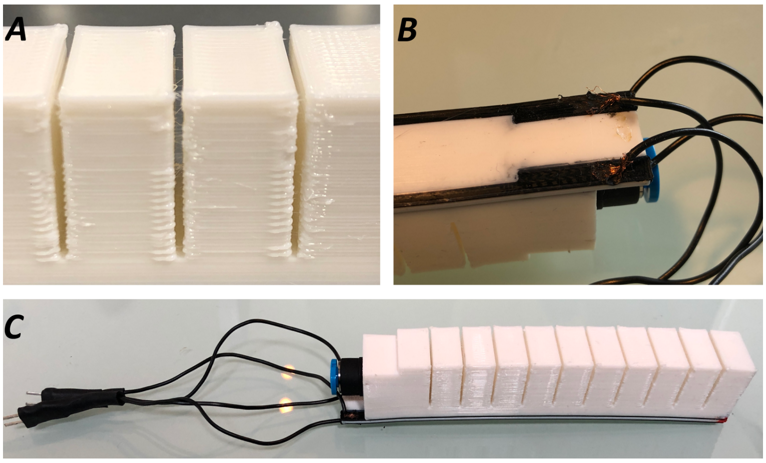

Figure 4.3: A. After printing stringing is present between the chambers. B. Detailed view of the wires melted into the mounting pads of the sensors. C. Actuator after post processing, including connector for the tube and wires connected to the mounting pads for the sensor readout.

4.3 Actuator Model

A lot of research has already been done in making analytical and numerical models of pneu-net actuators [33–36]. Numerical methods such as FEM have proven to be able to precisely determine the deflection of soft robotic actuators if the material properties are known [34]. These models require a substantial amount of computing power and are time consuming. This has the consequence that these models are not that useful for real-time applications [35].

For real-time applications analytical models are more useful. Different types of analytical models have already been made. However, these models are often complex. Wei Xiao et al. [36] have for example made a model of a pneu-net actuator, based on the minimum potential energy principle. This principle states that at low temperatures a body deforms or displaces to a position that minimises the total potential energy. Their model could determine the bending of their actuator precisely and had a maximum root mean squared error of 5 %.

Since the 3D printed actuator designed in this research has a complex shape and the material properties of the 3D printed structures are non-linear [16], precisely modelling the actuator would be a separate study. By simplifying the shape and making certain assumptions, a first attempt has been made in this section to model the actuator and the sensor.

4.3.1 Pneu-net Actuator Model

To model the actuator, the Euler–Bernoulli beam theory is used. The bottom part of the actuator is modelled as a cantilever beam with Young's modulus E, moment of inertia I, length L and with an bending moment M generated by the chambers [33], Figure 4.4 shows a schematic view of this beam. It is assumed that the beam only bends and therefore not expands in the axial direction. This means that the strain in the neutral axis can be assumed to be zero. It must be noted that the Euler–Bernoulli beam theory is only accurate for small deformations (Euler Bernoulli has a less than 5 % error for tip deflections up to 20 % of the initial length, but already a 20 % error for tip deflections of 40 % of the initial length [37]). The assumption of a constant Young's modulus is also not entirely correct since in general a TPU behaves as a hyperelastic material [16].

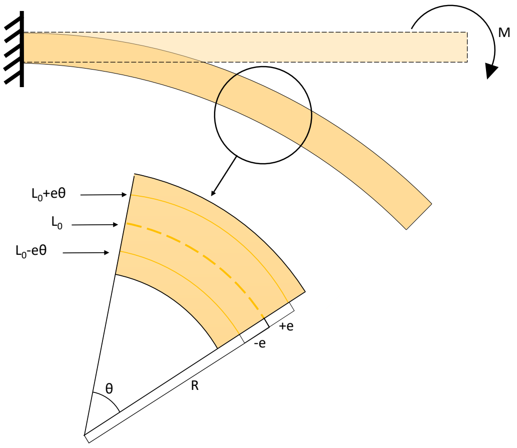

Figure 4.4: Schematic view of the bottom layer of the actuator modelled as a cantilever beam, with the strain sensors at a distance $+e$ and $-e$ from the neutral line. The chambers of the actuator generate a bending moment M.

Since the internal potential energy is uniformly distributed over the actuator, the actuator can be assumed to bend in a constant curvature with radius of curvature R [34]. Using the Euler-Bernoulli beam theory the relation between the momentum and radius of curvature is given as:

$$R = \frac{EI}{M} \tag{4.1}$$

Where, assuming that the beam does not expand in the axial direction, the momentum on the beam depends linearly on the applied pressure [33]. The bending angle θ can then be calculated using:

$$\theta = \frac{L}{R} \tag{4.2}$$

The radius of curvature and the bending angle thus depend linearly on the pressure inside the actuator.

4.3.2 Strain Gauge Model

When the radius of curvature and the bending angle of the actuator is known, also the strain in the sensors can be calculated. It is assumed that the top sensor is placed a distance e above the neutral axis and that the bottom sensor is placed a distance e below the neutral axis. The length of the top sensor in deflected state, L_d, is defined as [38]:

$$L_d = L_0 + e \cdot \theta \tag{4.3}$$

Thus the strain, ϵ, is given by:

$$\epsilon = \frac{\Delta L}{L_0} = \frac{L_d - L_0}{L_0} = \frac{L_0 + e \cdot \theta - L_0}{L_0} = \frac{e \cdot \theta}{L_0} \tag{4.4}$$

The strain in a strain gauge can be related to the change in resistance, $\frac{\Delta R}{R_0}$, using the gauge factor, GF [4]. For the top strain this results in:

$$\frac{\Delta R}{R_0} = \epsilon \cdot GF = \frac{e \cdot \theta}{L_0} \cdot GF \tag{4.5}$$

The equation for the bottom sensor is almost the same, only the distance from the neutral axis is now $-e$, which results in:

$$\frac{\Delta R}{R_0} = \epsilon \cdot GF = \frac{-e \cdot \theta}{L_0} \cdot GF \tag{4.6}$$

The gauge factor however is not constant for this 3D printed material, as explained in Section 4.3. Doshi et al. [39] have experimentally determined the relation between the strain and the resistance change for conductive TPU to be:

$$\frac{\Delta R}{R} = 2.356\varepsilon^2 - 1.408\varepsilon \tag{4.7}$$

This relation was determined for strain values between -0.1 to 0.4. This relation will be used in the model to determine the resistance change due to the strain in the sensors.

Using this simple model we can relate, under certain assumptions, the moment applied to the beam to the radius of curvature and the bending angle (equation 4.1 and 4.2). Using this angle the change in resistance of the two sensors can be calculated (equation 4.5 and 4.6).

4.4 Actuator Characterisation Method

The actuator needs to be pressurised to be able to bend. To do this the setup as seen in Figure 4.5 has been build. The green highlighted part is the pressure regulator part. The setup is based on the setup made by Caasenbrood et al. [40]. They have developed what they call a Soft Robotics Control Unit (SRC).

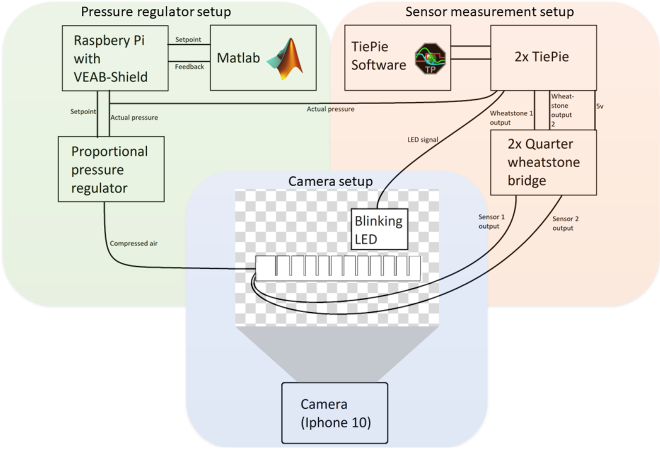

Figure 4.5: Measurement setup.

The main controller of the system is a Raspberry Pi 4 model B. Onto this Raspberry Pi a shield is placed, which is the interface between the Raspberry Pi and the pressure regulator. The used pressure regulator is a Festo three-way proportional pressure regulator (VEAB-L-26-D9-Q4-V1-1R1).

The Raspberry Pi is programmed using Python and can communicate with Matlab Simulink. In Simulink a controller is build using a simple feedback loop, in which a desired pressure can be programmed.

In order to characterise the bending behaviour of the actuator, the angle of the actuator is measured. This was done optically using a camera (Iphone 10, Apple, Cupertino, CA, USA) with a 4k resolution and a 60 Hz frame rate. The camera is placed on a tripod in front of the actuator and the actuator is placed in front of a paper with a chessboard pattern. For analysing the video and tracking the tip of the actuator, to later calculate the angle, Kinovea is used. Kinovea is a free video analysis tool. In Kinovea, first the chessboard pattern was used to set the scale, this scale is not needed if only the angle needs to be determined, but since also the shape of the whole actuator will be analysed, the exact dimensions are needed. Next the coordinate frame was set. Figure 4.6 illustrates how the coordinate frame is defined. The Y-axis is placed on the side wall of the base of the actuator and is defined positive in downwards direction. The X-axis is of course perpendicular to the Y-axis and is defined positive to the right. The origin is placed on the bottom sensor. The position of the bottom tip of the actuator is tracked and the angle is defined as the angle between the X-axis and the line going from the origin to the tip (blue line in Figure 4.6). Using simple geometry, the angle (θ, in radians) can be defined as:

$$\theta = \arctan(\frac{Y_{tip}}{X_{tip}}) \tag{4.8}$$

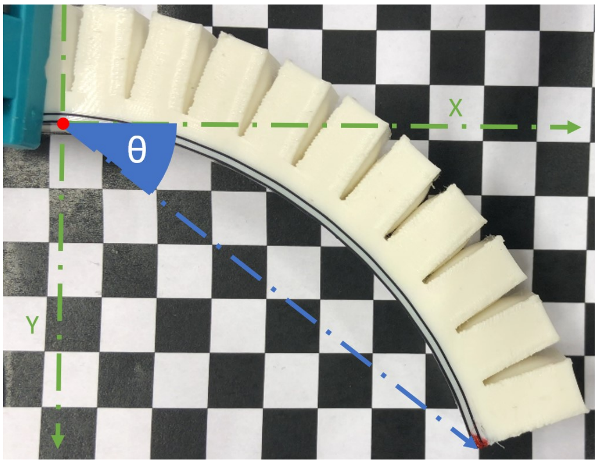

Figure 4.6: Used method to determine the angle (θ) of the actuator.

To analyse the behaviour of the actuator, multiple experiments have been done. First the actuator was pressurised to around 0.6 MPa (note that all pressure values are relative to the ambient pressure, e.g. 0.0 MPa in an experiment means that the pressure is equal to the ambient pressure), to analyse how the chambers expand and the actuator bends. Hereafter the dynamic response of the actuator was tested using a step response with a 0.3 MPa amplitude. In this experiment also the amount of leakage was tested by switching of the air supply after the step response to see how fast the actuator would bend back to its original shape.

Another experiment was used to determine the bending angle of the actuator due to an input pressure. In this experiment a triangular wave (0.0 MPa to 0.1 MPa, 0.5 rad/s) was applied to the actuator. Lastly the force produced by the tip of the actuator was determined. This was done by placing a force sensor (LCMFD-50N) under the tip of the actuator. The force produced by the actuator was measured from 0.0 MPa to 0.3 MPa for three different actuator angles (0°, 30° and 45°).

During these experiments, the pressure inside the actuator was logged (10 kHz sampling frequency) and the actuator was filmed (60 Hz frame rate). Using Kinovea the angle of the tip could be calculated and using Matlab the angle could be plotted against the pressure inside the actuator. The data recorded with the oscilloscope was filtered in Matlab using the Matlab lowpass function with an 8 Hz cut-off frequency. The data from the force sensors was filtered with a moving average filter (average taken over 5000 data points). The bending behaviour of the actuator was also compared to the modelled bending behaviour, using the model as described in Section 4.3.

4.5 Sensor Characterisation Method

In order to determine the angle of the actuator using the sensors, the sensor should first be characterised. In Section 4.3 it was determined that the change in resistance of the strain gauge is proportional to angle of the actuator using the gauge factor. So to determine the angle of the actuator, the change in resistance should be measured.

To do this a Wheatstone bridge was used [4]. For a differential measurement it would be the easiest to use a half-Wheatstone bridge. A schematic of a half-Wheatstone bridge can be seen in Figure 4.7.B. Using this type of circuit, the output signal would be the differential measurement of the two sensors. Since for this research it is also useful to see the individual change in resistance of each sensor, such that they can be compared to the differential signal, two quarter-Wheatstone bridges will be used. A quarter-Wheatstone bridge can be seen in Figure 4.7.A. The used bridges have a 5 V input signal. The output of each bridge is measured using a digital oscilloscope (Handyscope HS5, TiePie engineering, Sneek, the Netherlands). Between each bridge and the oscilloscope an amplifier (AD620) is placed, since the signal coming from the bridges is relatively small. Using the oscilloscope also the pressure inside the actuator is logged and using the signal generator available on the oscilloscope, a blinking LED is controlled. This LED is placed in the frame of the camera. The voltage measured from the LED and the camera recording of the LED are used to synchronise the camera output and the data coming from the oscilloscope. The total setup can be seen in Figure 4.5.

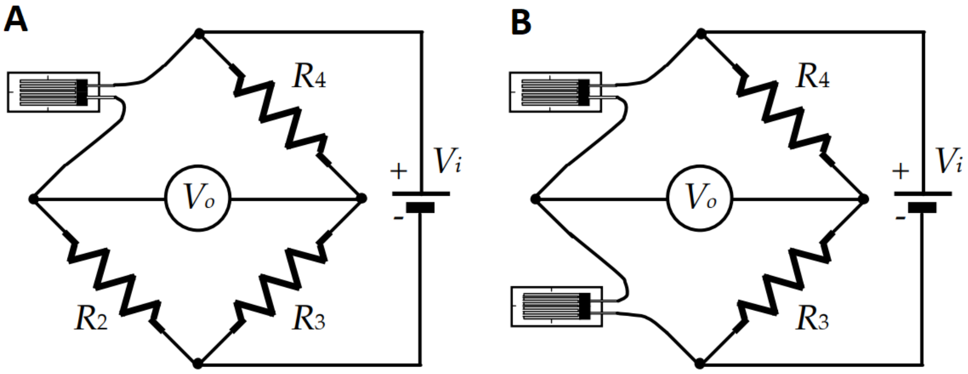

Figure 4.7: A. Quarter-Wheatstone bridge configuration (including one strain gauge) B. Half-Wheatstone bridge configuration (including two strain gauges) [41].

To characterise the sensors they were tested for multiple bending sequences of the actuator. A sinusoidal wave (0.0 MPa to 0.1 MPa, 0.5 rad/s) was applied to the actuator. The pressure inside the actuator and the output of both sensors was logged using the oscilloscope (10 kHz sampling frequency). The angle of the actuator was determined using the camera (60 Hz frame rate) and Kinovea. The logged data using the oscilloscope was filtered in Matlab using the Matlab lowpass function with an 8 Hz cut-off frequency. This has been done, both for actuator one and for actuator two, such that the sensor output of the actuators can be compared. The output from the sensors will is also compared with the modelled sensor output using the model as explained in Section 4.4.

4.6 Conclusion

In this chapter the methods used to fabricate and characterise the sensing structure have been explained. It has been decided to print the actuator from NinjaFlex TPU and the sensor from PI-eTPU 85-700+. The whole structure has been 3D-printed in one-go using the Diabase H-series FFF printer. To calculate the expected bending behaviour, a simple analytical model of the actuator with embedded sensor has been made. This model relates the change in resistance to the bending angle. Lastly, in this chapter the characterisation methods have been described. The used setup can be seen in Figure 4.5. This setup is used to characterise both the actuator and the sensor.

5 Results

5.1 Introduction

In this chapter the results of the different experiments will be presented and the results will be analysed such that the actuator and sensor can be characterised. First the results for the actuator characterisation will be presented, after which the results for the sensor characterisation will be presented.

5.2 Actuator Characterisation

In Figure 5.1 the actuator can be seen with an applied pressure of approximately 0.6 MPa. The actuator is capable of bending approximately 180° for this pressure. Figure 5.1.A and 5.1.B show how the walls between the chambers expand and push against each other causing the actuator to bend. They also show that the other walls do not expand considerably, which is beneficial for the efficiency of the actuator as explained in Section 2.5.

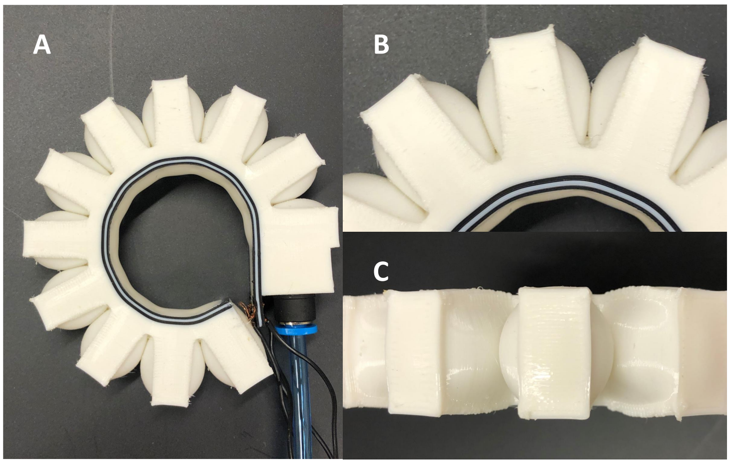

Figure 5.1: A. Side view of the pressurised actuator ($P \approx 0.6$ MPa. B. Detailed side view. C. Detailed top view.

To test the dynamic response of the actuator, a step function with a 0.3 MPa amplitude was applied to the actuator. In Figure 5.2 the resulting bending angle can be seen. The step signal was applied at $t = 1$ s. Due to this step function the actuator bent to approximately 100°. To characterise a step response, the time constant (τ) can be calculated. For this step response the time constant was calculated to be: $\tau_1 = 0.27$ s. To test the amount of air leakage out of the actuator, the supply of air was switched off after the step response at $t \approx 10$ s and the air could only escape because of the 3D printed actuator not being completely airtight. Figure 5.2 shows that after switching off the air supply, the actuator bends back to almost its original angle. The time constant for this response was determined to be $\tau_2 = 1.88$ s

Figure 5.3 shows the correlation between the input pressure and the resulting angle of the actuator. The input pressure was a triangular wave (0 MPa to 0.1 MPa, 0.5 rad/s). The pressure-angle relation looks like to be reasonably linear, however the actuator angle is lower for bending than for contracting.

Figure 5.4 shows the force produced by the actuator. This force is measured at the tip and is plotted over the pressure inside the actuator. The force was measured for three different angles of the actuator (0°, 30° and 45°). A linear relation between the pressure and the force can be seen. The slope of this relation appears to be lower for higher actuator angles.

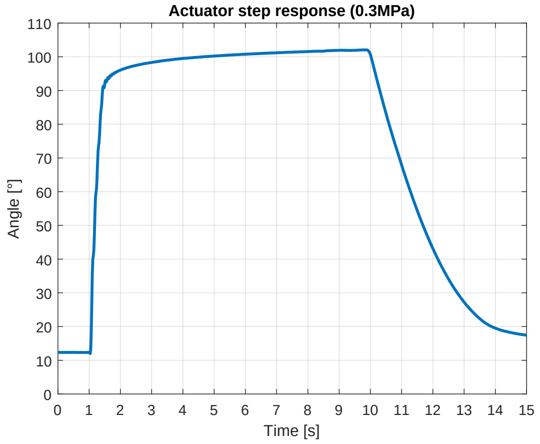

Figure 5.2: Step response of the actuator (at $t = 1\,\text{s}$ $P = 0.3\,\text{MPa}$, at $t \approx 10\,\text{s}$ the air supply is switched off).

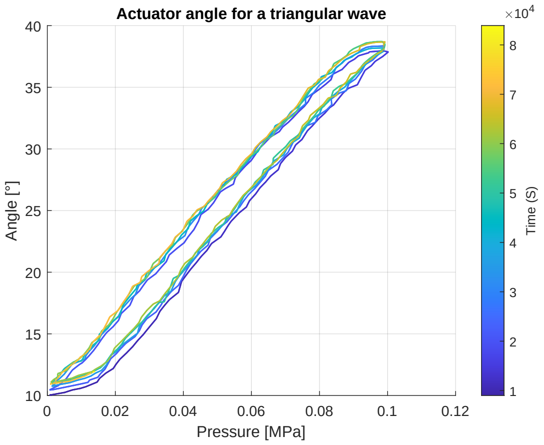

Figure 5.3: Actuator angle [°] over pressure [MPa], for a triangular input pressure (0 MPa to 0.1 MPa, 3 rad/s

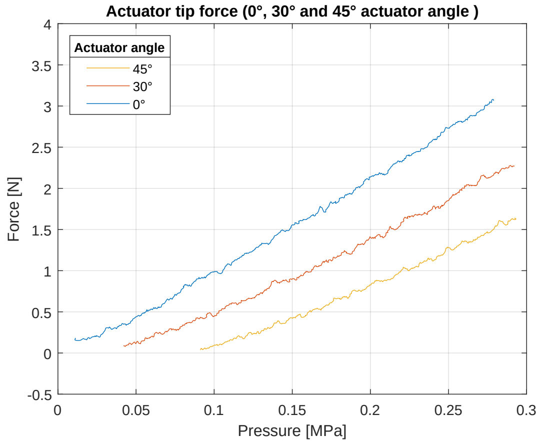

Figure 5.4: Actuator output force (measured at the tip) [N] over input pressure [MPa] (0 MPa to 0.3 MPa).

Table 5.1: Measured resistance of the sensors and mutual resistance between the sensors for the 2 different actuators

	R_0 **(top)** (kΩ)	R_0 **(bottom)** (kΩ)	R_0 **(mutual)** (MΩ)
Actuator 1	5.05	8.20	2.05
Actuator 2	5.01	7.80	~ 10.00

5.3 Sensor Characterisation

First, the initial resistance (R_0) of the sensors was measured for actuator one and two. The measured resistance of the sensors and the mutual resistance between the sensors is shown in Table 5.1. The resistance of the top and bottom sensor is in the range of a few kΩ. The bottom sensor has an initial resistance which is about twice the top sensor. The mutual resistance is more than two orders of magnitude larger than the resistance of the sensor, which means that the sensors are reasonable electrically isolated from each other.

Next the dynamic response of the sensors is tested. Figure 5.5 shows the time domain response of the top sensor (channel 1, CH1) and bottom sensor (channel 2, CH2) of actuator one for a sinusoidal input pressure. In Figure 5.5 also the differential signal can be seen, which is the difference between the two sensor outputs (CH1-CH2). In Figure 5.6 the same plot can be seen, but now for actuator two. Figure 5.5 and 5.6 show that the change in resistance of the top sensor is mainly negative and the change in resistance of the bottom sensor is mainly positive. The differential signal shows a stronger relation with the bending angle, than the individual signal of both the top sensor and the bottom sensor.

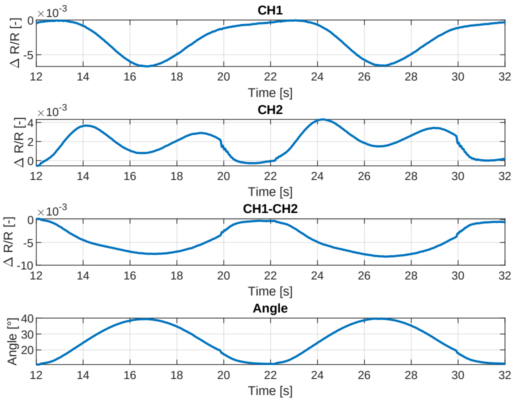

Figure 5.5: Actuator one: Relative resistance change [-] of CH1, CH2, CH1-CH2 and the angle of the actuator over time [s] (0 MPa to 0.1 MPa, 0.5 rad/s).

In order to better understand the response of the sensors. The output of the two sensors and the differential signal, have been plotted over the angle of the actuator. Figure 5.7 shows the resulting plot for actuator one and Figure 5.8 shows the resulting plot for actuator two. For both actuators the output of the differential signal is more linear than the output of the individual sensors.

5.4 Model Validation

In order to validate the model, the bending behaviour of the pneu-net has been compared to the cantilever beam model (as explained in section 4.3). In Figure 5.9 the position of actuator one (tracked over the whole length in between in the two sensors) has been plotted for multiple pressure levels (0 MPa to 0.5 MPa). The estimated position by the model has been plotted on

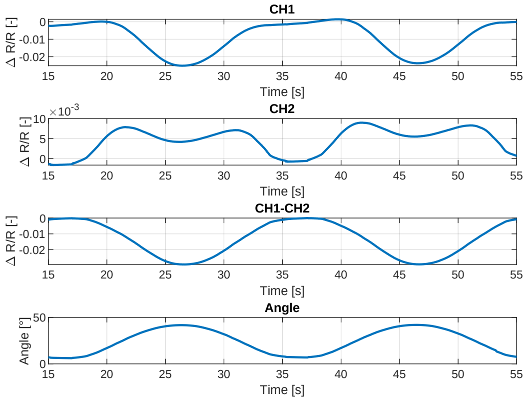

Figure 5.6: Actuator two: Relative resistance change [-] of CH1, CH2, CH1-CH2 and the angle of the actuator over time [s] (0 MPa to 0.1 MPa, 0.25 rad/s).

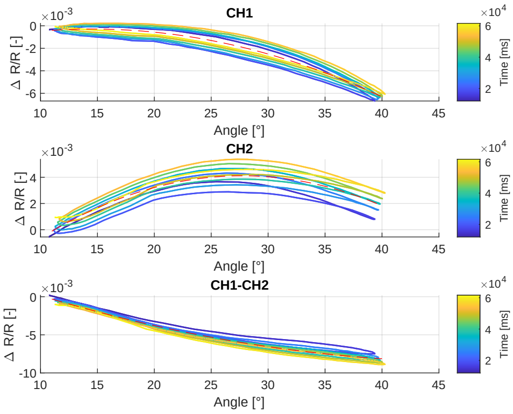

Figure 5.7: Actuator one: Relative resistance change [-] of CH1, CH2, CH1-CH2 over the actuator angle [°] including second-order fit (0 MPa to 0.1 MPa, 0.5 rad/s).

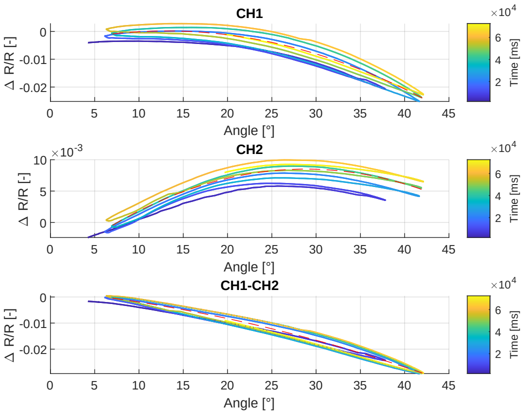

Figure 5.8: Actuator two: Relative resistance change [-] of CH1, CH2, CH1-CH2 over the actuator angle [°] including second-order fit (0 MPa to 0.1 MPa, 0.25 rad/s).

this data. The model starts in the origin, the definition of the origin was explained in Section 4.4 and can be seen in Figure 4.6. The value for $\frac{M}{EI}$ was chosen such that the model would best fit the data. In Figure 5.10 the used values for $\frac{M}{EI}$ can be seen. Onto these values a linear fit was plotted, where the value for $\frac{M}{EI}$ at $P = 0.0$ MPa was not taken into account since for this pressure the actuator angle should be zero. This is not the case since the actuator already has an initial angle of around 8° when not pressurised. For the other values of $\frac{M}{EI}$ it can be seen that the relation between $\frac{M}{EI}$ and the pressure is approximately linear.

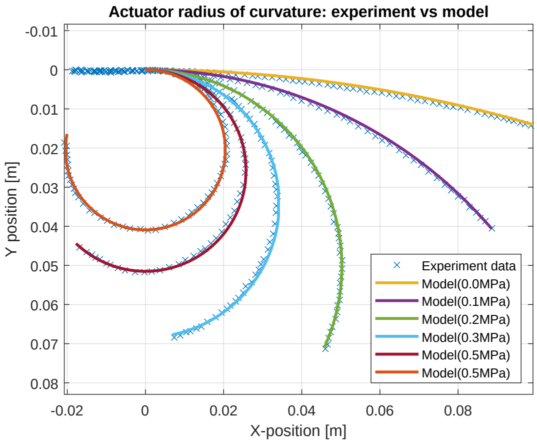

Figure 5.9: Modelled actuator position vs measured actuator position.

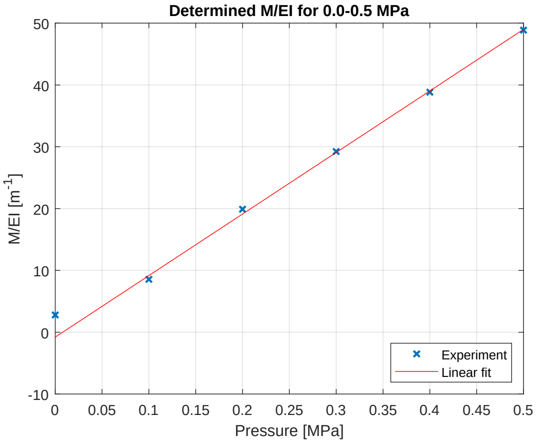

Figure 5.10: Used values of $\frac{M}{EI}$ in Figure 5.9. A linear fit has been plotted onto the data points (the first data point is excluded from this fit).

Lastly, the measured sensor output has been compared to the modelled sensor output. Using the model as explained in section 4.3, the expected sensor output could be plotted. This output has been compared to the lines that are fitted onto the data of Figure 5.7 and 5.8. The fitted lines have been vertically shifted such that they all start at zero for a 10° angle. For the model, the neutral axis is assumed to be in the middle of the bottom layers for both actuators. The modelled and measured sensor output for actuator one can be seen in Figure 5.11, and for actuator two in Figure 5.12.

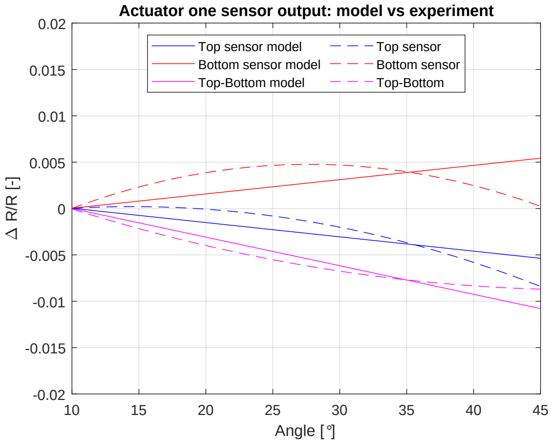

Figure 5.11: Sensor output determined by the model compared to the fit of Figure 5.7.

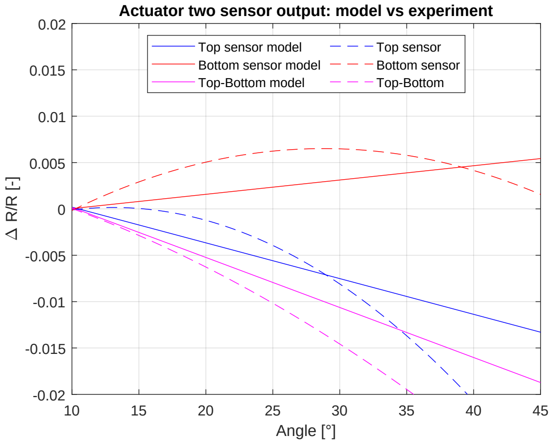

Figure 5.12: Sensor output determined by the model compared to the fit of Figure 5.8.

5.5 Conclusion

The results from the different experiments have been presented in this chapter. In Figure 5.1 the actuator can be seen in actuated state, which shows that the actuator is capable of bending approximately 180°. However, the step response shows that the actuator has some leakage. The force produced by the actuator has been determined to be linearly dependent on the applied pressure and is maximum 3 N for an input pressure of 0.3 MPa. The sensors have also been characterised. The time response of the sensors of actuator one for a sinusoidal input can be seen in Figure 5.5 and for actuator two in Figure 5.6. The response of the sensors has also been plotted over the angle (Figure 5.7 for actuator one and Figure 5.8 for actuator two). These plots show that the differential signal improves the linearity of the sensor response.

6 Discussion

6.1 Introduction

In this chapter the results of the actuator and sensor characterisation, as presented in the previous chapter will be discussed. Furthermore, the model will be discussed and its assumptions will be analysed. Lastly, the limitations of this study will be discussed.

6.2 Actuator Characterisation

The designed and printed actuator is leaking. Figure 5.2 shows that the actuator is losing pressure when the air supply is stopped. This leaking is caused by two main problems. First of all, the actuator is leaking at the connector. The connector is pushed in the printed actuator and has a rubber o-ring. Still some air escapes in between the connector and the actuator wall. This is probably caused by the rough surface finish of the printed hole caused by the 3D printing process. This might be solved by gluing the tube into the actuator. The actuator is also leaking at the chamber walls. Especially the thin walls (2 perimeters, 0.8 mm) in between the chambers have some small voids through which air is leaking out. These small holes form during the manufacturing process. When a small bit of filament sticks to the extruder during printing. This bit of filament can get dropped later during the process onto a traxel and can cause defects in the traxels. These defects can form into small voids. By testing, the slicer settings were found which gave the most air tight actuator (Table 4.1). Although the actuator is still leaking, The resulting actuator is air tight enough to be used/characterised. There are sealing methods available [42], however these sealants are not flexible enough to be used on TPU. Making the walls thicker has also been found to decrease the amount of leakage, however, this has the consequence that it takes more pressure and thus energy for the actuator to bend. Maybe heating treating the printed actuators at high temperatures (higher than the 80° used in this paper) could help annealing the traxels together and close any voids.

Figure 5.3 shows that the bending angle of the actuator is almost linearly dependent on the input pressure. The pneu-net angle is however lower for bending than for contracting. This is known as hysteresis. Hysteresis in elastomers is believed to be a consequences of the viscoelastic or visoplastic nature of the elastomer and corresponds to the amount of energy lost during a cycle [43]. Figure 5.3 also shows the maximum angle is getting bigger over time, this is known as the Mullins effect. Ogden et al. [44] stated that the Mullins effect is the effect that the stress-strain curve depends on the maximum loading previously encountered (also sometimes called cyclic softening or stress softening [43]).

Figure 5.4 shows that the tip of the actuator is capable of producing a force of approximately 3 N when pressurised to ~0.28 MPa. For larger actuator angles the produced force is lower, since a certain amount of energy is lost in bending the actuator to this angle.

6.3 Sensor Characterisation

The measured initial resistance of the sensors is shown in Table 5.1. Clearly the bottom sensor has a higher initial resistance than the top sensor. Schouten et al. [5] also saw this effect in their sensor. They think this is due to the fact that the bottom sensor is printed on the heated bed while the top sensor is printed on a layer of NinjaFlex TPU. The first layer which is printed on the bed, is often printed on a slightly different layer height. This problem could be solved by first printing one layer of support material or Ninjaflex TPU, before starting the fabrication process of the actuator.

The response of the sensing structure of actuator one is shown in Figure 5.5. The top sensor of the actuator shows a drop in resistance, this is expected since this sensor is positively

Table 6.1: Coefficient of determination (R-squared) for both sensing structures, for both a linear and a second order fit

	Linear fit	**Second order fit**
Actuator one: top sensor	0.860	0.949
Actuator one: bottom sensor	0.227	0.795
Actuator one: top-bottom sensor	0.955	0.978
Actuator two: top sensor	0.820	0.951
Actuator two: bottom sensor	0.503	0.919
Actuator two: top-bottom sensor	0.972	0.983

strained when the actuator is bent and for positive strain the resistance of the conductive TPU drops as explained in Section 3.4. The bottom sensor which experiences a negative strain for bending shows an increase in resistance which drops again for larger bending angles. The differential signal shows a close relation with the bending angle. In Figure 5.7 the sensor response has been plotted against the angle of the actuator. Clearly the differential signal shows a more linear response than the individual sensors. These figures also shows that the measured resistance of the top and bottom sensor gets higher over time. This effect is known as softening behaviour [22]. Normally, most softening behaviour can be seen in the first cycle, but due to the measurement setup, the first cycle was not recorded correctly. Just like the actuator, the sensor output also shows hysteresis. Hysteresis is often seen in sensor made of conductive TPU. It is caused by the settling time of the material needed when going back to the zero strain situation. The hysteresis is partially removed by doing a differential measurement. Some of the softening behaviour and in general drift, is also removed by the differential measurement.

The response of the sensing structure of actuator two closely resembles the response of actuator one (Figure 5.6 and 5.8). However, the response of the top sensor of actuator two is approximately two times larger than the response of the top sensor of actuator one. This also influences the differential signal. The higher response of the top sensor causes the differential line to slightly bend downwards for higher actuator angles (20° to 45°). This two times larger response of the top sensor of actuator two, seems to confirm that the neutral axis of the actuator is closely to the middle of the bottom layer. Since the top sensor of actuator two was also placed two times a distance e from the middle of the bottom layer, while the top sensor of actuator one was placed at a distance e from the middle of the bottom layer.

To quantify the linearity of the measured sensor response, the coefficient of determination (R^2) has been determined for the sensors of both actuators for a linear fit and a second order fit, these values can be found in Table 6.1. The coefficient of determination is a number between zero and one, that measures how well a fit can predict an outcome. A coefficient of determination of one would mean that the fit would perfectly fit all the data. When analysing Table 6.1 a clear difference can be seen between the individual sensor responses and the differential response. The coefficient of variability is both for the linear fit and the second order fit higher for the differential response. This confirms that the differential response can better determine the angle of the actuator. For the differential response, the second order fit has a slightly higher coefficient of variability. The second order model is thus better at predicting the angle, although the difference is small. This small difference between the first and second order model, confirms that the response of the differential signal hardly has any second order term and is thus rather linear. The difference between the coefficient of variability of the differential response of actuator one and two is neglectable.

6.4 Model

To model the actuator and sensing structure, the Euler Bernoulli beam theory is used. Figure 5.9 shows that the assumption of a constant radius (which depends on the applied pressure) is probably correct. While the Euler Bernoulli beam theory can only be used for small actuator angles (less than 5% error for tip deflections up to 20% of the initial length [37]), 5.10 still shows a linear relation between the applied pressure and the value of $\frac{M}{EI}$. If the pressure inside the actuator is the same as the ambient pressure (P=0.0 MPa), the expected bending angle would be zero. This is however not the case. This is either due to the actuator being plastically deformed or having a really long settling time after already being used for several cycles.

The modelled sensor output shows some relation with the measured output. For actuator one, the modelled response is close to the actual response. However for large deflections the response of the individual sensors shows a second order response. It is not exactly known why this happens. A possible explanation could be that the actuator is also expanding in the axial direction while the modelled beam is assumed to stay at a constant length. This expansion would be removed by the differential measurement as explained in Section 3.4. This behaviour is confirmed by the differential signal, which clearly has a smaller second order term. The error between the measured and modelled response could also be because of the other assumptions and limitations of the model. It is assumed that the modelled beam has a constant Young's modules which in general for TPU is not the case [16]. The Euler Bernoulli beam theory is also only accurate for small deflections. Applying it on this actuator which has large deflections (over 90°) results in a error (over 20% [37]). For future research it is advised to look into more complex models which are valid for large deflections [33, 35, 36], which take the hyperelastic properties of the material into account and which also account for small axial deformations.

6.5 Limitations

The used setup (Figure 4.5) has some limitations. The angle of the actuator was determined by recording the actuator and later analysing the recordings in Kinovea. This method induced multiple errors. First of all, the coordinate frame is placed manually in Kinovea, the position of this coordinate frame is based on the wall of the first chamber. While this has been done carefully, having it not perfectly on this wall can cause a systematic error in the measured angle. The tracking algorithm also sometimes failed to exactly follow the tip of the actuator and adjustments by hand needed to be done. Later, it was found that the tracking algorithm worked better if the actuator was placed on a blank paper instead of a chessboard pattern. Still the determined position of the tip was not always correct. Lastly, the synchronisation of the camera data and the data from the oscilloscope was difficult to achieve. The Blinking LED was used to synchronise the data, but since the camera has a 60 Hz frame rate and the sampling rate from the oscilloscope is 10 kHz, the synchronisation was limited by the camera frame rate. Having the oscilloscope data and the determined angle not synchronised can have odd effects on the data.

The used used load cell (LCMFD-50N) can only measure force in one degree of freedom. During the force measurements the actuator bent a bit causing the tip of the actuator to move. Because of this the direction of the force was not constant during the experiment. While the position of the force sensor was carefully chosen, it could still be that the measured force is smaller than the actual force. This problem could be solved by using a force sensor which can measure forces in multiple degrees of freedom.

The obtained sensor response also has some limitations. The sensor has only been tested to around 45°. It is not known what the sensor response will be for higher angles. The sensor has also only been tested for low strain rates. Wolterink et al. [4] noticed that for conductive TPU the gauge factor is dependent on the strain rate. This is something that has often been seen, especially in conductive rubbers [45, 46]. It is not known what the response of this sensing structure will be for higher strain rates.

As earlier explained in Section 2.5, this pneu-net design is probably not the most energy efficient design. The goal for this research was to embed a 3D printed sensing structure in a 3D printed actuator. The focus was thus put on 3D printing an actuator which was airtight enough to be test, and not on designing the most energy efficient actuator. Now that it is known that these pneu-nets can be 3D printed using NinjaFlex TPU, the design could be optimised in a future research to be more energy efficient or to be able to bend to a desired radius of curvature or bending angle. Finite element models or analytical models could be useful when determining the best dimensions [33–36].

6.6 Conclusion

The actuator characterisation shows that the actuator is capable of bending approximately 180°. The actuator response shows however hysteresis and cyclic softening. The differential measurement has a positive effect on the obtained response of the sensing structure. However, also the sensor shows some hysteresis. The model has some relation with the obtained response of the sensor, but due to the simplification and assumptions in the model, the modelled response does not match perfectly with the data. Lastly the used setup can be improved since multiple errors could have been induced because of the setup.

7 Conclusion

This work demonstrates a working concept of a 3D printed soft robotic actuator with embedded sensing. The designed (pneu-net) actuator is capable of bending approximately 180° ($P \approx 0.6\,\text{MPa}$) and can apply a force of around 3 N for 0.3 MPa. A sensing structure, which consist of two strain gauges made from carbon doped TPU, has successfully been embedded in the actuator. The actuator and sensing structure can be printed in one go using a multi material FFF printer. The differential signal of the embedded sensing structure shows an almost linear relation to the bending angle, while the response of each individual sensor is non-linear due to the nature of carbon doped TPU.

Making a model of these actuators is however still difficult. The proposed model highly simplifies the pneu-net actuator and models it as a cantilever Euler Bernoulli beam. The Euler Bernoulli beam theory is however only accurate for small deflections. The deflections of this beam are too large and thus the modelled sensor output is different than the measured sensor output, especially for higher bending angles. Making a more accurate model of the actuator would be useful for better understanding of the sensor response.

Nevertheless, it has been proven that 3D printing can be used to low cost manufacture this type of actuator with embed sensing structure. It allows the structure to be easily customised for all kind of applications. Still, work can be done in further optimising these actuators and sensing structures, e.g. making the actuator more air tight and removing the hysteresis from the sensor response.

Based on this research a paper has been written for the IEEE SENSORS 2022 conference. This paper can be found in appendix A

A IEEE SENSORS 2022 paper

Based on this research a paper has been written for the IEEE SENSORS 2022 conference. This is a conference where scientists can present their latest research findings, ideas, and applications in the areas of sensors and sensing technologies [47].

The paper is titled: ’3D Printed Soft Robotic Actuator With Embedded Strain Sensing For Position Estimation’ and is written by Gerjan Wolterink, Stijn Kolkman and Gijs Krijnen. The paper can be found below.

3D Printed Soft Robotic Actuator With Embedded Strain Sensing For Position Estimation

Gerjan Wolterink, Stijn Kolkman, Gijs Krijnen
Robotics And Mechatronics group, University of Twente, Enschede, The Netherlands,
Email: gerjan.wolterink@utwente.nl

***Abstract* - This work shows the development and characterization of a fully 3D printed pneumatic soft robotic actuator with embedded strain gauges to estimate the bending angle of the actuator. The actuator was printed in one go using a multi material Fused Filament Fabrication (FFF) printer. By taking the difference of the reading of two integrated strain gauges, printed using carbon doped TPU, a strong linear realtion ($R^2 = 0.97$) between the bending angle and sensor output is achieved.**

Keywords - 3D Printing, Sensorized, Soft Actuators, Pneu-net, Strain sensor, Conductive TPU

I. INTRODUCTION

Sensorization of soft robotics actuators allows for safe control of soft robots and enables (co)-operating in close proximity to humans. Information about the soft robotic's interaction forces with the environment allows e.g. for the development of haptic feedback for tele-operation. Furthermore, sensorized soft robotic actuators may provide real-time information about the deformation of the soft robot to update its control strategy [1].

A common type of soft robotic actuators are the so called ”pneu-nets”, actuated by pressurising a network of elastic chambers [2]. 3D printing these pneu-net actuators increases the design freedom, allowing for highly customizable functional structures and automation of the process, eliminating the need for the manual fabrication using molds [3]–[5].

The emerging development of 3D printing technologies and materials facilitates the creation of soft and flexible sensors that can be integrated into functional structures [6], [7]. Elgeneidy et al. [4] have presented a fully FDM printable soft actuator based on a pneu-net design with an embedded strain sensor to provide bending and simple contact feedback. Although both the sensor and the actuator are fully 3D printed there was still a manual fabrication step to combine the sensor with the actuator. Furthermore, the use of a single strain sensor resulted in high hysteresis. This may be expected since soft polymer 3D printed strain sensors commonly show strong non-linear behaviour [7]. These effects cam be highly reduced by taking the differential signal of two oppositely positioned strain gauges [8]. Therefore, this work introduces and characterizes a fully 3D printed sensorized pneumatic soft robotic actuator with two integrated strain gauges printed in one go using a multi-material FFF 3D printer.

II. METHODOLOGY

A. Actuator design

The actuator design was based on a pneu-net design by Mosadegh et al. [2], [9] and was further optimized for fabrication using an FFF 3D printer (see Figure 1). The total size of the actuator was $107.6 \times 14.4 \times 18.8$ mm ($L \times W \times H$). The actuator consists of 11 chambers with an inner dimension of $6.4 \times 11.2 \times 15.4$ mm. The wall thickness was 1.6 mm and 0.8 mm between the chamber to increase bending of the actuator. The bottom part of the actuator is 1.8 mm thick and contains the two strain gauges, one at the top and one at the bottom. Each strain gauge is 0.6 mm thick (4 layers), has a width of 1.6 mm (4 traxels) and circumferences the outside of the bottom part of the actuator. The left corner of Figure 1 shows the definition of the bending angle (θ) of the actuator.

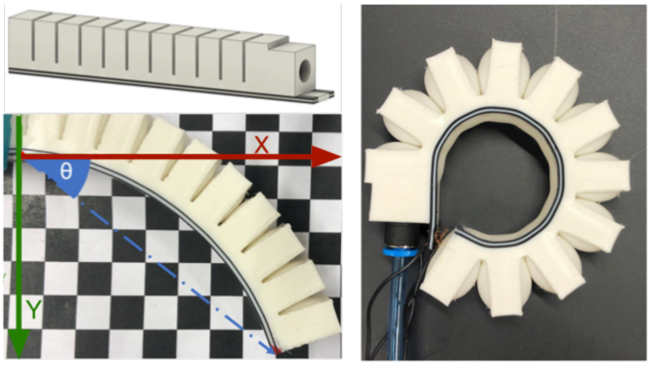

Fig. 1. Top left: CAD model of the actuator. The two black lines are the strain gauges. Bottom left: Definition of the bending angle (θ). Right: Actuator in its maximal bending state ($P \approx 0.6$ MPa).

B. Fabrication

The model was sliced (Simplify 3D, Inc., USA) in layers of 0.150 mm with 3 perimeters. The actuators are printed in one go using a multi-material 3D printer (Diabase H-Series Hybrid, Diabase Engineering, USA) fitted with 0.4 mm nozzles (Bondtech LGX, Bondtech AB, Sweden). No support was used in the overhangs due to the relative small distance of maximal 11.2 mm. The base material of the actuator is non-conductive thermoplastic polyurethane (TPU) (NinjaFlex

---

This work was supported by the Dutch Soft Robotics Consortium of the 4TU Federation.

SemiFlex, Fenner Drives, USA) and the strain gauges are fabricated using a carbon black infused TPU (PI-ETPU 85-700+, Palmiga Innovation, Sweden). Connections to the strain gauges are made by melting in a fine stranded wire. The pneumatic connection is made using a push connection (FESTO Cartridge QSPK10-4).

C. Characterization

The pressure to the actuator is provided using the Soft Robotics Control Unit developed by Caasenbrood et al. [10]. This system consists of a custom-made shield placed on a Raspberry Pi 4 that is connected to a proportional pressure regulator (Festo, VEAB-L-26-D13-Q4- V1-1R1). The Raspberry Pi communicates with a PC running a Simulink (Mathworks Inc., USA) interface to set the pressure. The strain gauges were individually connected in a quarter bridge configuration comparable to [11], of which the voltage was measured using an instrumentation amplifier (AD620, Analog Devices, USA). Subsequently this data is logged using a digital oscilloscope (Handyscope HS5, TiePie engineering, The Netherlands). The same oscilloscopes were also used to log the pressure sensor of the pressure regulator and to blink an LED. This blinking LED was used to synchronize a video (captured at 60 Hz) taken of the actuator with the recording of the scope. Using motion analysis software (Kinovea) the bending angle (as indicated in Figure 1) is obtained.

To analyze the bending angle of the actuator with respect to the pressure, the actuator was pressurized using a triangular wave (0-0.1 MPa, at 3 rad s^{-1}) for 6 cycles. The first cycle was removed from the data set since the slope of the applied pressure deviates from the other five cycles. The force was measured using a load cell (LCMFD-50N, Omega Engineering, USA) positioned under the actuator tip. This load cell was connected to the USB oscilloscope via a load-cell amplifier (IAA100, Futek, USA). The force was measured from 0 MPa to 0.5 MPa at angles of 30° and 45°. The data of the strain gauges was low pass filtered at 8 Hzusing the Matlab filter function. Subsequently, $\Delta R/R$ was determined using the initial resistance of the strain gauges.

III. RESULTS

Figure 2 shows the resulting bending angle at a sudden pressure of 0.3 MPa applied at $t = 1$ s at $t \approx 10$ s the air supply is switched off. The air could only escape due to leaks in the actuator.

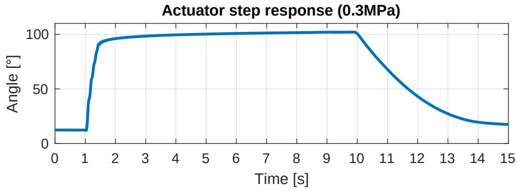

Fig. 2. Step response of the actuator at $t = 1$ s $P = 0.3$ MPa, at $t \approx 10$ s the air supply is switched off.

Figure 3 shows the correlation between the input pressure and the angle of the actuator for a triangular wave with an amplitude of 0.1 MPa and a period of 3 rad s^{-1} and for the situation in which there is no load. The force of the actuator at a static position with respect to the pressure is shown in Figure 4. The tip force of the actuator shows a reasonable linear relation with the applied pressure. However, the amount of force decreases with increasing bending angle.

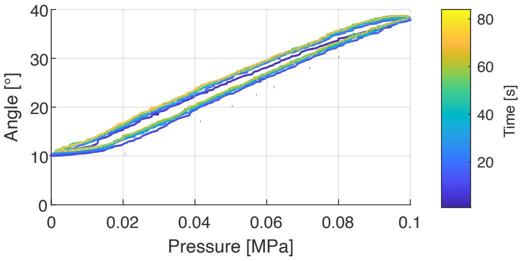

Fig. 3. Actuator angle over pressure, traiangular wave input of 3 rad s^{-1}.

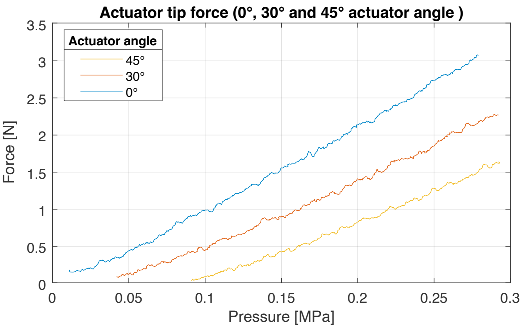

Fig. 4. Actuator output force (measured at the tip) over input pressure.

The resistance of the 3D printed strain sensors are 5.01 k■ for the top (CH1) and 7.80 k■ for the bottom (CH2) sensor. The responses of these sensors over time to the bending angle are shown in Figure 5. The relative resistance change versus the angle over multiple periods is shown in Figure 6. The top sensor shows a strong drop in resistance especially after 20°, the bottom sensor show a strong increase in resistance till approximately 25° followed by a slow decline in resistance. The difference between the two sensors, shown in the bottom graph of Figure 6, shows a more linear relationship and less hysteresis with respect to the bending angle.

Figure 7 shows that force applied by the tip of the actuator decreases with increasing bending angle. The differential signal of the two strain gauges decreases with increasing force till 2.5 N after which a strong increase is visible in the 0° position. The sensors output decreases with increasing force in the 30° situation but increases when the actuator is in a static 45° angle.

IV. DISCUSSION

The 3D printed soft robotic actuator shows some air leaks as shown in Figure 2. However, these leaks where small enough

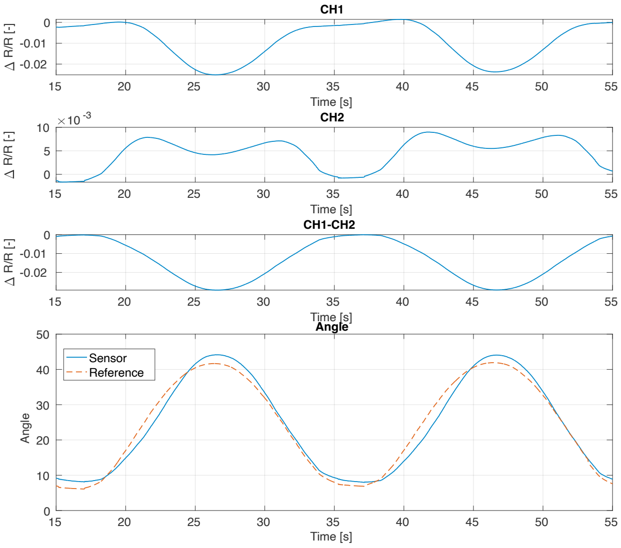

Fig. 5. Relative resistance change of CH1, CH2, CH1-CH2, angle of actuator over time estimated using a linear fit on CH1-CH2 and reference angle.

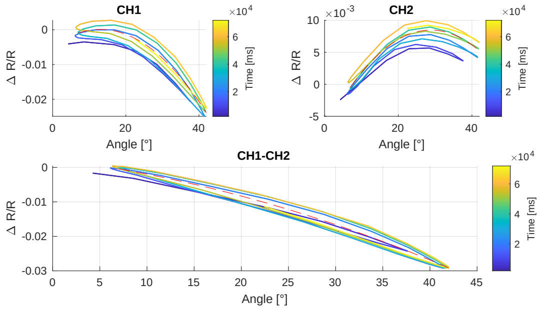

Fig. 6. Relative resistance change of the top (CH1) bottom (CH2) and difference (CH1-CH2) of the strain gauges with respect to the bending angle.

to be compensated by the air flow. The leaks are mainly present around the pneumatic connector and at the two perimeter wide parts of the pneumatic chamber. Further optimizing the printing process and pattern might overcome these issues [3]. The first loop of the bending angle versus the actuator pressure (Figure 3) shows a lower bending angle with respect to the subsequent load cycles.

Although the actuator tip is kept at constant position while determining the actuator force (Figure 4) the actuator was still able to deform due to the applied force. In e.g. the 0° angle situation this resulted in an S-shaped curvature of the actuator and the associated strain. Furthermore, the total length of the actuator might increase with increasing pressure.

Using carbon doped TPU materials as piezoresistive sensing material comes at the cost of many nonlinearirties due to viscoelastic properties and physical processes in the matrix of the composite material [11]. However, as expected the differential signal between the bottom and top sensor results in a more linear relative resistance change versus bending angle relationship [8]. Additional compensation algorithms might be used to further improve linearity and limit hysteresis [7], [12].

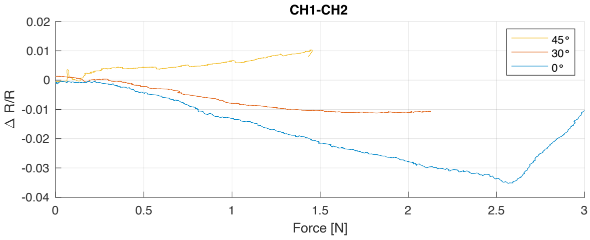

Fig. 7. Actuator output force and the differential resistance change in 30° and 45° position.

For the sensing part the actuator can be roughly approximated by a cantilever beam with strain gauges placed below and above the neutral axis. Therefore, the top part will be extended and the bottom part compressed during bending. Carbon doped TPU materials typically show first a strong decline of the resistivity at low strain (< 0.25) followed by an increase of the resistivity [11]. The top sensor in Figure 6 shows this decline indicating low strains due to extension of the sensor. The bottom shows an increase due to compression since this sensor is placed below the neutral axis.

The sudden increase of the differential signal of the two strain gauges after 2.5 N in the 0° position, as shown in Figure 7, might also be the result of the same effect on the resistivity of carbon doped TPU at low strain. In the 45° position the strain gauges might be pre-strained to such an extent that only an increase in resistance is shown.

The differential signal of the strain gauges shows a strong linear relation ($R^2 = 0.97$) when there are no external forces acting on the actuator. Future research is needed to study the effect of the expected crosstalk of external forces and if, potentially with the placement of more strain gauges, the bending angle and interaction forces could be estimated. More accurate models predicting the bending of the actuator might help to better understand the strain in the sensing structures. Coupling such models with the feedback of the actuator position might provide the mismatch between the expected and actual position potentially allowing for interaction force prediction. Embedding sensors will potentially result in improved feedback controlled actuators increasingly enabling safe control of soft robots and (co)-operation with humans.

V. CONCLUSIONS

This works shows a working concept of a 3D printed soft robotic actuator with embedded sensing that is printed in one go. By taking the differential signal of the two embedded strain gauges a strong linear relation ($R^2 = 0.97$) can be achieved in a bending angle ranging from 5° to 45° with no external load on the actuator.

ACKNOWLEDGMENT

The authors would like to thank Femke van Beek, Chu Khanh Hoang and Brandon Caasenbrood for the development and their support of the Soft Robotics Control Unit.

REFERENCES

[1] K. Elgeneidy, N. Lohse, and M. Jackson, “Bending angle prediction and control of soft pneumatic actuators with embedded flex sensors – A data-driven approach,” *Mechatronics*, vol. 50, no. October 2017, pp. 234–247, 2018. [Online]. Available: https://doi.org/10.1016/j.mechatronics.2017.10.005

[2] B. Mosadegh, P. Polygerinos, C. Keplinger, S. Wennstedt, R. F. Shepherd, U. Gupta, J. Shim, K. Bertoldi, C. J. Walsh, and G. M. Whitesides, “Pneumatic networks for soft robotics that actuate rapidly,” *Advanced Functional Materials*, vol. 24, no. 15, pp. 2163–2170, 2014.

[3] G. Stano, L. Arleo, and G. Percoco, “Additive manufacturing for soft robotics: Design and fabrication of airtight, monolithic bending PneuNets with embedded air connectors,” *Micromachines*, vol. 11, no. 5, 2020.

[4] K. Elgeneidy, G. Neumann, M. Jackson, and N. Lohse, “Directly printable flexible strain sensors for bending and contact feedback of soft actuators,” *Frontiers Robotics AI*, vol. 5, no. FEB, pp. 1–14, 2018.

[5] M. Manns, J. Morales, and P. Frohn, “Additive manufacturing of silicon based PneuNets as soft robotic actuators,” *Procedia CIRP*, vol. 72, pp. 328–333, 2018. [Online]. Available: https://doi.org/10.1016/j.procir.2018.03.186

[6] M. Schouten, G. Wolterink, A. Dijkshoorn, D. Kosmas, S. Stramigioli, and G. Krijnen, “A Review of Extrusion-Based 3D Printing for the Fabrication of Electro-and Biomechanical Sensors,” *IEEE Sensors Journal*, no. AUGUST, pp. 1–12, 2020.

[7] G. Wolterink, D. Kosmas, M. Schouten, B. J. Van Beijnum, P. Veltink, and G. Krijnen, “Evaluation of A 3D Printed Soft Sensor for Measuring Fingertip Interaction Forces,” *IEEE Sensors Journal*, vol. 22, no. 12, pp. 11 499–11 508, 2022.

[8] M. Schouten, B. Prakken, R. Sanders, and G. Krijnen, “Linearisation of a 3D printed flexible tactile sensor based on piezoresistive sensing,” *Proceedings of IEEE Sensors*, vol. 2019-Octob, pp. 2019–2022, 2019.

[9] Harvard Biodesign Lab, “Soft Robotics Toolkit,” 2018. [Online]. Available: https://softroboticstoolkit.com/

[10] B. J. Caasenbrood, F. E. Van Beek, H. K. Chu, and I. A. Kuling, “A Desktop-sized Platform for Real-time Control Applications of Pneumatic Soft Robots,” *2022 IEEE 5th International Conference on Soft Robotics, RoboSoft 2022*, pp. 217–223, 2022.

[11] G. Wolterink, R. Sanders, B.-J. B. J. van Beijnum, P. Veltink, and G. Krijnen, “A 3d-printed soft fingertip sensor for providing information about normal and shear components of interaction forces,” *Sensors*, vol. 21, no. 13, pp. 1–13, jul 2021.

[12] D. Kosmas, M. Schouten, and G. Krijnen, “Hysteresis Compensation of 3D Printed Sensors by a Power Law Model with Reduced Parameters,” in *FLEPS 2020 - IEEE International Conference on Flexible and Printable Sensors and Systems, Proceedings*, 2020.

Bibliography

[1] "Dutch soft robotics · 4tu." `https://dutchsoftrobotics.nl/`. (accessed: 16.03.2022).

[2] M. Schouten, G. Wolterink, A. Dijkshoorn, D. Kosmas, S. Stramigioli, and G. Krijnen, "A review of extrusion-based 3d printing for the fabrication of electro-and biomechanical sensors," *IEEE Sensors Journal*, 12 2020.

[3] A. Abbas and J. Zhao, "Twisted and coiled sensor for shape estimation of soft robots," *2017 IEEE/RSJ International Conference on Intelligent Robots and Systems (IROS)*, pp. 482–487, 2017.

[4] G. Wolterink, R. Sanders, B.-J. van Beijnum, P. Veltink, and G. Krijnen, "A 3d-printed soft fingertip sensor for providing information about normal and shear components of interaction forces," *Sensors*, vol. 21, no. 13, 2021.

[5] M. Schouten, B. Prakken, R. Sanders, and G. Krijnen, "Linearisation of a 3d printed flexible tactile sensor based on piezoresistive sensing," in *2019 IEEE SENSORS*, pp. 1–4, 2019.

[6] K. Elgeneidy, G. Neumann, M. Jackson, and N. Lohse, "Directly printable flexible strain sensors for bending and contact feedback of soft actuators," *Frontiers in Robotics and AI*, vol. 5, 2018.

[7] N. El-Atab, R. B. Mishra, F. Al-Modaf, L. Joharji, A. A. Alsharif, H. Alamoudi, M. Diaz, N. Qaiser, and M. M. Hussain, "Soft actuators for soft robotic applications: A review," *Advanced Intelligent Systems*, vol. 2, 2020.

[8] M. Franke, A. Ehrenhofer, S. Lahiri, E.-F. M. Henke, T. Wallmersperger, and A. Richter, "Dielectric elastomer actuator driven soft robotic structures with bioinspired skeletal and muscular reinforcement," *Frontiers in Robotics and AI*, vol. 7, 2020.

[9] J.-W. Sohn and S.-B. Choi, "Various robots made from piezoelectric materials and electroactive polymers: A review," *International Journal of Mechanical Systems Engineering*, vol. 3, no. 1, 2017.

[10] H.-J. Chung, A. M. Parsons, and L. Zheng, "Magnetically controlled soft robotics utilizing elastomers and gels in actuation: A review," *Advanced Intelligent Systems*, vol. 3, no. 3, p. 2000186, 2021.

[11] Z. Ren, M. Zarepoor, X. Huang, A. P. Sabelhaus, and C. Majidi, "Shape memory alloy (sma) actuator with embedded liquid metal curvature sensor for closed-loop control," *Frontiers in Robotics and AI*, vol. 8, 2021.

[12] M. Yang, Z. Yuan, J. Liu, Z. Fang, L. Fang, D. Yu, and Q. Li, "Photoresponsive actuators built from carbon-based soft materials," *Advanced Optical Materials*, vol. 7, no. 16, p. 1900069, 2019.

[13] M. S. Xavier, C. D. Tawk, A. Zolfagharian, J. Pinskier, D. Howard, T. Young, J. Lai, S. M. Harrison, Y. K. Yong, M. Bodaghi, and A. J. Fleming, "Soft pneumatic actuators: A review of design, fabrication, modeling, sensing, control and applications," *IEEE Access*, vol. 10, pp. 59442–59485, 2022.

[14] B. Mosadegh, P. Polygerinos, C. Keplinger, S. W. Wennstedt, R. F. Shepherd, U. Gupta, J. Shim, K. Bertoldi, C. J. Walsh, and G. M. Whitesides, "Pneumatic networks for soft robotics that actuate rapidly," *Advanced Functional Materials*, vol. 24, 2014.

[15] H. B. Lab, "Soft robotics toolkit." `https://softroboticstoolkit.com/`. (accessed: 24-05-2022).

[16] C.-H. Liu, Y. Chen, and S.-Y. Yang, "Quantification of hyperelastic material parameters for a 3d-printed thermoplastic elastomer with different infill percentages," *Materials Today Communications*, vol. 26, p. 101895, 2021.

[17] Y. Sun, Q. Zhang, X. Chen, and H. Chen, "An optimum design method of pneu-net actuators for trajectory matching utilizing a bending model and ga," *Mathematical Problems in Engineering*, vol. 2019, Oct 2019.

[18] X. Wang, Y. Cheng, H. Zheng, Y. Li, and C. Wang, "Design and optimization of actuator for soft bionic finger," *2021 4th International Conference on Intelligent Autonomous Systems (ICoIAS)*, pp. 260–264, 05 2021.

[19] J. F. Christ, N. Aliheidari, P. Pötschke, and A. Ameli, "Bidirectional and stretchable piezoresistive sensors enabled by multimaterial 3d printing of carbon nanotube/thermoplastic polyurethane nanocomposites," *Polymers*, vol. 11, no. 1, 2019.

[20] G. Wolterink, D. Kosmas, M. Schouten, B.-J. Van Beijnum, P. Veltink, and G. Krijnen, "Evaluation of a 3d printed soft sensor for measuring fingertip interaction forces," *IEEE Sensors Journal*, pp. 1–1, 2022.

[21] D. Kosmas, M. Schouten, and G. Krijnen, "Hysteresis compensation of 3d printed sensors by a power law model with reduced parameters," in *2020 IEEE International Conference on Flexible and Printable Sensors and Systems (FLEPS)*, pp. 1–4, 2020.

[22] M. Schouten, R. Sanders, and G. Krijnen, "3d printed flexible capacitive force sensor with a simple micro-controller based readout," in *2017 IEEE SENSORS*, pp. 1–3, 2017.

[23] H. Jin, S. Jung, J. Kim, S. Heo, J. Lim, W. Park, H. Y. Chu, F. Bien, and K. Park, "Stretchable dual-capacitor multi-sensor for touch-curvature-pressure-strain sensing," *Scientific Reports*, vol. 7, 2017.

[24] H. Jonkers, "3d printed electronics," *MSC assignment, University of Twente*, jan 2022.

[25] P. Flowers, C. Reyes, S. Ye, M. J. Kim, and B. Wiley, "3d printing electronic components and circuits with conductive thermoplastic filament," *Additive Manufacturing*, vol. 18, 10 2017.

[26] M. Saari, B. Cox, E. Richer, P. Krueger, and A. Cohen, "Fiber encapsulation additive manufacturing: An enabling technology for 3d printing of electromechanical devices and robotic components," *3D Printing and Additive Manufacturing*, vol. 2, 03 2015.

[27] M. Kisic, N. Blaz, L. Zivanov, and M. Damnjanovic, "Elastomer based force sensor fabricated by 3d additive manufacturing," *AIP Advances*, vol. 10, no. 1, p. 015017, 2020.

[28] *Strain Gauge*, ch. 72, pp. 544–550. John Wiley & Sons, Ltd, 2009.

[29] P. Regtien, F. van der Heijden, M. Korsten, and W. Olthius, "Chapter 3 - measurement errors and uncertainty," in *Measurement Science for Engineers* (P. Regtien, F. van der Heijden, M. Korsten, and W. Olthius, eds.), pp. 43–85, Oxford: Butterworth-Heinemann, 2004.

[30] NinjaTek, "Ninjaflex® 3d printing filament, technical specifications." https://ninjatek.com/wp-content/uploads/NinjaFlex-TDS.pdf, 2016. (accessed: 16.03.2022).

[31] P. innovation, "Palmiga innovation." https://palmiga.com/. (accessed: 16.03.2022).

[32] "Autodesk fusion 360." https://fusion.online.autodesk.com/. (accessed: 15.06.2022).

[33] G. Alici, T. Canty, R. Mutlu, W. Hu, and V. Sencadas, "Modeling and experimental evaluation of bending behavior of soft pneumatic actuators made of discrete actuation chambers," *Soft Robotics*, vol. 5, no. 1, pp. 24–35, 2018.

[34] M. S. Xavier, A. J. Fleming, and Y. K. Yong, "Finite element modeling of soft fluidic actuators: Overview and recent developments," *Advanced Intelligent Systems*, vol. 3, no. 2, p. 2000187, 2021.

[35] C. Rad, O. Hancu, and C. Lapusan, "Data-driven kinematic model of pneunets bending actuators for soft grasping tasks," *Actuators*, vol. 11, no. 2, 2022.

[36] W. Xiao, D. Hu, G. Yang, and C. Jiang, "Modeling and analysis of soft robotic surfaces actuated by pneumatic network bending actuators," *Smart Materials and Structures*, vol. 31, p. 055001, mar 2022.

[37] J. Oberhammer, A.-q. Liu, and G. Stemme, "Time-efficient quasi-static algorithm for simulation of complex single-sided clamped electrostatic actuators," *Microelectromechanical Systems, Journal of*, vol. 16, pp. 373 – 382, 05 2007.

[38] R. van den Berg, "Qualitative flow sensing with 3d-printed sensors for application in a robotic bird," *BSC assignment, University of Twente*, jun 2021.

[39] A. Doshi, "3d printed interaction force sensors for robotic fingers," *MSC assignment, University of Twente*, May 2021.

[40] B. J. Caasenbrood, F. E. van Beek, H. K. Chu, and I. A. Kuling, "A desktop-sized platform for real-time control applications of pneumatic soft robots," in *2022 IEEE 5th International Conference on Soft Robotics (RoboSoft)*, pp. 217–223, 2022.

[41] F. Dezi, F. Gara, and D. Roia, *Dynamic Characterization of Open-ended Pipe Piles in Marine Environment*, ch. 3, p. 177. IntechOpen, 09 2016.

[42] "Comparison of sealing methods for fdm materials." https://stratasis.com/. (accessed: 29.06.2022).

[43] S. Cantournet, R. Desmorat, and J. Besson, "Mullins effect and cyclic stress softening of filled elastomers by internal sliding and friction thermodynamics model," *International Journal of Solids and Structures*, vol. 46, no. 11, pp. 2255–2264, 2009.

[44] R. W. Ogden and D. G. Roxburgh, "A pseudo–elastic model for the mullins effect in filled rubber," *Proceedings of the Royal Society of London. Series A: Mathematical, Physical and Engineering Sciences*, vol. 455, no. 1988, p. 2861–2877, 1999.

[45] K. Sau, T. Chaki, and D. Khastgir, "The effect of compressive strain and stress on electrical conductivity of conductive rubber composites," *Rubber Chemistry and Technology*, vol. 73, pp. 310–324, 05 2000.

[46] N. Das, T. Chaki, and D. Khastgir, “Effect of axial stretching on electrical resistivity of short carbon fibre and carbon black filled conductive rubber composites,” *Polymer International*, vol. 51, no. 2, pp. 156–163, 2002.

[47] “Ieee sensors 2022.” `https://2022.ieee-sensorsconference.org/`. (accessed: 04.07.2022).